MINIATURE HOURGLASS SHAPED ACTUATOR GEOMETRY STUDY USING A FINITE ELEMENT SIMULATION

A Thesis

by

ROSTON CLEMENT ELWELL

Submitted to the Office of Graduate Studies of
Texas A&M University
in partial fulfillment of the requirements for the degree of

MASTER OF SCIENCE

May 2010

Major Subject: Mechanical Engineering

MINIATURE HOURGLASS SHAPED ACTUATOR GEOMETRY STUDY USING A FINITE ELEMENT SIMULATION

A Thesis

by

ROSTON CLEMENT ELWELL

Submitted to the Office of Graduate Studies of
Texas A&M University
in partial fulfillment of the requirements for the degree of

MASTER OF SCIENCE

Approved by:

Chair of Committee,	Terry Creasy
Committee Members,	Alan Palazzolo
	Ramesh Talreja
Head of Department,	Dennis O'Neal

May 2010

Major Subject: Mechanical Engineering

ABSTRACT

Miniature Hourglass Shaped Actuator Geometry Study Using a Finite Element Simulation. (May 2010)

Roston Clement Elwell, B.S., California State Polytechnic University, Pomona

Chair of Advisory Committee: Dr. Terry Creasy

This project investigated a miniature, hourglass-shaped actuator (MHA) and how its geometry affects performance. A custom, self-contained, finite-element simulation code predicts how each MHA deforms when pressurized internally.

This analysis describes the MHA geometry's effects on four characteristics: a) work density b) mechanical advantage, c) work advantage and d) percent elongation. The first three characteristics are compared to a traditional actuator operating at the same pressure and elongation.

A finite-element modeling code was tailored to study the MHA at 5 MPa internal pressure when 1) MHA height and side-wall thickness are constant and side-wall arc length varies; 2) MHA side-wall arc length and thickness are constant and the height varies; and 3) MHA side-wall thickness varies while height and side-wall arc length are fixed. Case 3 was studied using the MHA geometry with the highest work density found in either condition 1 or 2.

Peak mechanical advantage, 6.47, occurs in a constant height MHA—Case 1—when the side-wall arc length is shortest. Highest elongation, 8.67%, occurs in the Case 1 MHA with the longest side-wall arc length. Finally, under Case 3, work density reaches 0.434 MJ/m^3 when the side-wall thickness is 1.9 mm.

The MHA has potential for active structures because its work density is high—higher than traditional actuators with the same elongation. Their small elongations limit their use; however, much work remains to determine how MHAs might be arranged in a useful array. Never the less, morphing airfoils and other active structures might benefit from embedded MHAs.

DEDICATION

To my father and mother, Richard and Martha Elwell

ACKNOWLEDGEMENTS

I express my appreciation to my committee chair, Dr. Terry S. Creasy, and my committee members, Dr. Alan Palazzlo, and Dr. Ramesh Talreja, for everything that they have taught me, both in and out of the classroom and what they have allowed me to teach myself. Gregory Payette was also a valuable and willing resource to me, and I am grateful to him.

My appreciation also goes to the Department of Mechanical Engineering at Texas A&M University for providing the opportunity for me to further my education. I also want to extend my gratitude to the DARPA which provided the funds for my research based upon work supported by DARPA and the US Army Research, Development and Engineering Command under contract W911W6-04-C-0069. Any opinions, findings, and conclusions or recommendations expressed in this material are those of the author and do not necessarily reflect the views of the US Army Research, Development and Engineering Command.

TABLE OF CONTENTS

Page

Page

Page

LIST OF FIGURES

Page

Page

Page

Page

LIST OF TABLES

Page

1. INTRODUCTION

1.1 Overview

This study looked at Miniature Hourglass shaped Actuator (MHA) behavior based on the MHA's geometry to understand their capabilities and limits as synthetic nastic materials, which are promising replacements for traditional actuators. The finite-element code surveyed three cases with varying MHA geometry. The MHA geometry is defined by five parameters: the arc angle, α; arc radius, r; arc wall thickness, t; the distance from the MHA's centerline to the center of the side-wall /end-wall intersection, R; and end thickness, T. Figure 1 identifies these parameters.

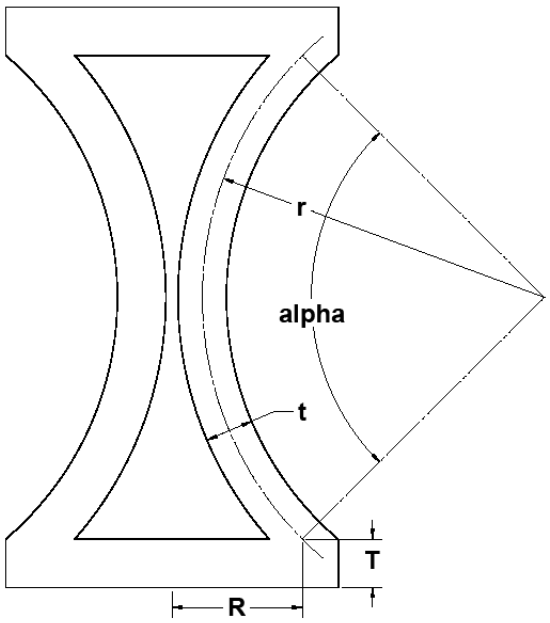

Figure 1. Five parameters define the MHA's shape. The MHA geometry is defined by the arc angle, α, arc radius, r, arc wall thickness, t, the distance from MHA center line to the intersection of the center of side-wall with the MHA bottom , R, and end thickness, T.

This thesis follows the style of *Advanced Materials.*

.

The MHA's structural material will affect the MHA's function, but materials selection is outside this study's scope. The baseline analysis here is directed toward nastic materials that use MHAs formed from a flexible thermoplastic. Because the MHA must operate reversibly for 100s to 1000s of cycles, the material model is linear elastic—no plastic deformation occurs. The MHA structural material's elastic modulus is 2.0 GPa, and its Poisson's ratio is 0.30. These material properties are similar to nylon, and McCutcheon[1] used these properties in a previous study of fluid-solid interaction in an MHA material with an arbitrary geometry. These properties might not describe a specific material, but they are close to the properties of flexible thermoplastics.

To create aircraft that perform better, it is necessary to advance the materials and systems used on aircraft The goal is to obtain a synthetic nastic material based on a machine-augmented composite (MAC) by embedding MHAs in a matrix to create a composite that is both actuator and structure to replace traditional actuation and structural systems that are discrete. By having the actuators embedded in the material it might be possible to create airfoils that are lighter and have many degrees of freedom. This increase in degrees of freedom comes from distributing microactuators in multiple orientations to increase the ways that actuated control system can actuate them. If there are enough actuators, an airfoil that's entire structure morphs might become possible.

The actuator design investigated here uses internal pressure to inflate a long, miniature machine with an hourglass-shaped cross section, which called an MHA. An isometric sketch showing the MHA geometry appears in Figure 2.

The finite element code that predicts MHA's response to internal pressure runs in Matlab. The code contains a mesh that generator specific to the MHA's geometry. The finite element model uses solid, continuum elements with an updated Lagrangian formulation. The elements are nine-node quadratic. The three-dimensional problem becomes two-dimensional by approximating the strain state as plane strain. This works because the miniature hourglass actuator is long in the out-of-plane direction, and because there is no load that induces strain out-of-plane.

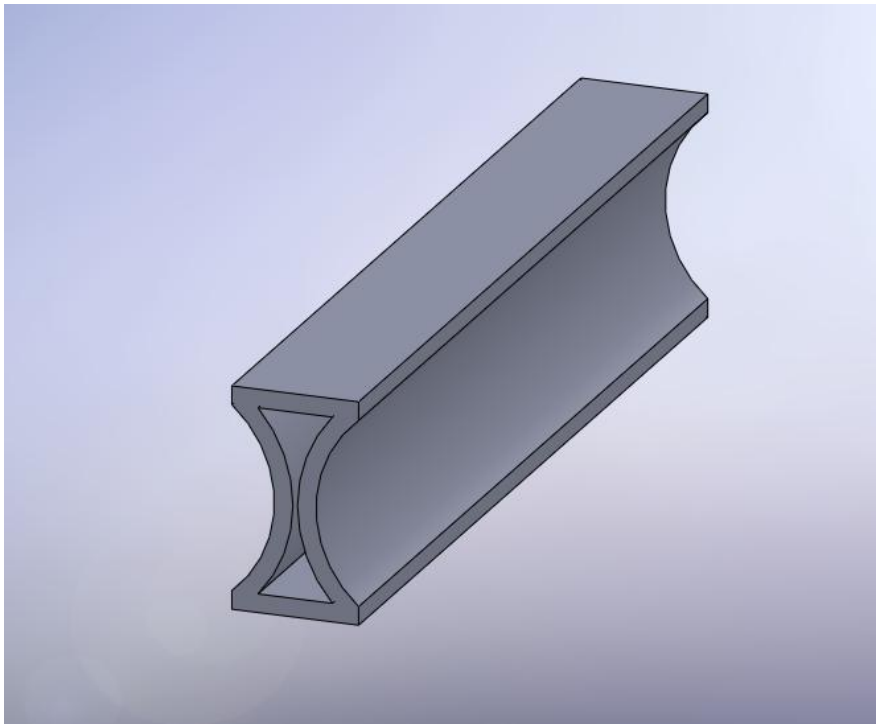

Figure 2. Isometric view of the undeformed MHA that is long in the out of plane direction. When pressurized, the side-walls move out and the cross-section elongates.

The finite element code is unitless; the user must assure the input is in consistent units. Here, length is in millimeters (mm) and load in Newtons (N), which yields pressure and elastic moduli in megapascals (MPa).

1.2 Objective

The program objectives are to 1) find the extremes in free strain, blocked stress, and work density available from the MHA profiles; and 2) to provide software that allows someone designing synthetic nastic materials a method to optimize the shape and material for a specific application within those extremes.

For the MHA to be implemented in a valuable way it is important to understand the MHA performance and to have a way to compare it to other actuators. Throughout this study the MHA will be contrasted with a Comparable Traditional Actuator (CTA). A CTA is a typical hydraulic or pneumatic actuator operating with a force from the pressure that is equal to the force from the pressure acting on the end surface of the MHA. For the CTA the strain is limited to the strain of the MHA. See Figure 3 for an illustration of this concept.

It is important to understand that the strain or percent elongation of the CTA ε_{CTA} is limited to the strain or percent elongation that the MHA ε_{MHA} can undergo. This is shown by the relation given in equation (1).

$$\varepsilon_{CTA} = \varepsilon_{MHA} \tag{1}$$

The force in the CTA is equal to the 5 MPa internal pressure times the area of the of the MHA end surface, $\mathbf{A}_{MHA}$. This is reiterated in equation (2).

$$F_{CTA} = P_{MHA} A_{MHA} \tag{2}$$

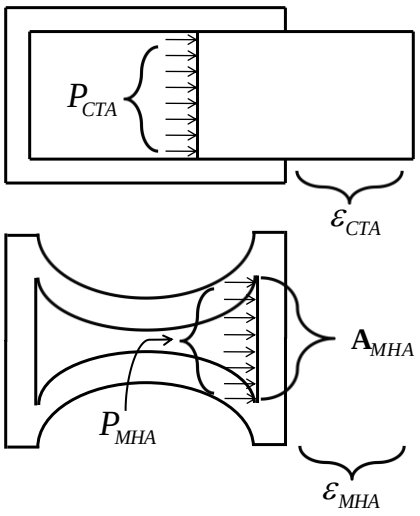

Figure 3. A Comparable Traditional Actuator (CTA) is a piston inside of a cylinder where the force from the pressure acting on the piston is equal to the force from pressure acting on the flat end surface of the Miniature Hourglass Shaped Actuator (MHA). The strain or percent elongation is set to be equal so that the work performed by each can be compared.

It is valuable to be able to see were the MHA performance would lie compared to other actuators. Figure 4 recreated from Huber et al[2] shows the actuation stress and actuation strain for many types of actuators. Different MHA geometries would lie on different places on this chart. The range for actuation stress would be from about 10^{1} to $10^{1.5}$ MPa and the range for actuation strain would be about 10^{-2} to 10^{-1}. This range is shown in Figure 4 as the square labeled MHA range. The actuation stress in the illustration is the blocked stress which means is the force an actuator can supply under no elongation and the actuation strain is the free strain or the elongation that the actuator can reach if it is allowed to freely expand. Unlike a hydraulic actuator and MHA cannot supply the blocked stress all the way to free strain. The force the MHA can supply decreases with elongation.

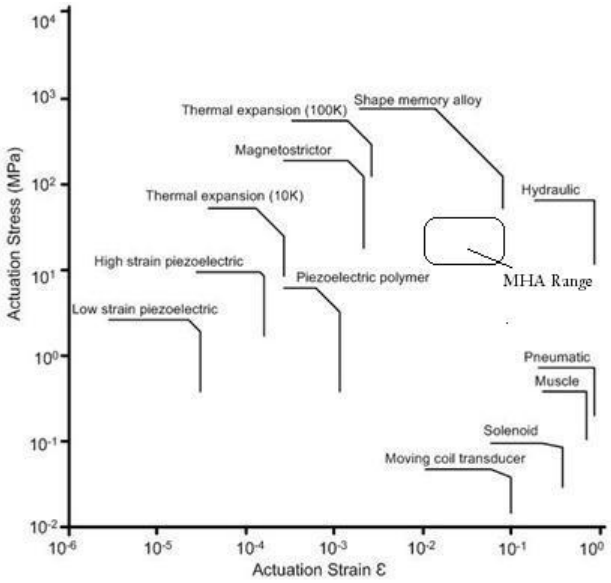

Figure 4. Actuator performance chart (Recreated from Huber et al[2]) shows actuation stress – actuation strain relationship for many different kinds of actuators. The MHA would appear in the region labeled MHA Range.

2. LITERATURE REVIEW

The research focus is to simulate small actuators that could be included in a structure, for example, a wing, to create a structure that morphs when the actuators fill with internal pressure. Because the goal is shape-changing structure, a broad spectrum of literature is reviewed. The relevant literature starts with an introduction to multifunctional materials with natural and synthetic multifunctional materials summarized. The discussion of natural multifunctional materials includes both animal and plant structures. Then the discussion turns to synthetic multifunctional materials--more specifically, shape changing and morphing materials—and ends with morphing wing concepts with potential MHA applications. This review provides a basis for discussing the miniature, hourglass-shape actuators.

2.1 Multifunctional Materials

Multifunctional materials must perform more than one function. They usually provide structure—to support loads—along with one or more additional functions. Multifunctional materials are found in nature; when studied, they can inspire synthetic multifunctional material design. Lee and Inman[3] define multifunctional materials and provide a brief history that tells how this material class grew out of the previous smart, or intelligent material concept. They state that a multifunctional material combines structural integrity with an abilities to actuate when stimulated, to sense the simulation, and to decide wheither it should respond. Some specific functionalities that could be added to conventional materials are vibration mitigation, power storage, crack remediation, and thermal management. Lee and Inman [3] also present their vision that

multifunctional materials could gain an increased ability to perform self-regulating and self-regenerating functions. These functions could be things like self-sensing, actuation, self-healing, self-cooling, and self-reconfiguration.

Christodoulou and Venables [4] highlighted the wide spectrum of design opportunities for what could be revolutionary material systems in their overview of ongoing activity in multifunctional materials development. They also introduce some challenges in creating synthetic multifunctional materials. Defining a synthetic multifunctional material system as a structural material that is able to carry mechanical loads and to exhibit an additional function that contributes to system performance, they group them in four categories: structural power material systems; autosensing and actuating material systems; electromagnetic multifunctional material systems; and survivable damage-tolerant material systems.

Multifunctional materials are an exciting and promising research area and advances in the ability to design and create these multifunctional materials will lead to advancements in industries that implement these materials. The aerospace industry is an obvious place because it continuously works to save weight, increase performance, and increase efficiency. As the technology gets better and implementation becomes available, these materials will reach a broader range of industries.

2.1.1 Natural Multifunctional Materials

Structures that use internal pressure to power movement are not new. Many plants use the turgor pressure generated by osmosis to power their movement. There are many structures in nature that change shape using internal pressure to create a localized

volume change that forces a shape change. Plants are a good example of how this works, so a brief overview of nastic motions and two example plants are presented.

These are Mimosa pudica, which is called the sensitive plant, and Dionea muscipula—the Venus flytrap. Hill and Findlay [5] summarize plant movements and present examples. Figure 5, which was recreated from one given in their paper The Power of Movements in Plants: The Role of Osmotic Machines, shows grouped movements and specific examples.

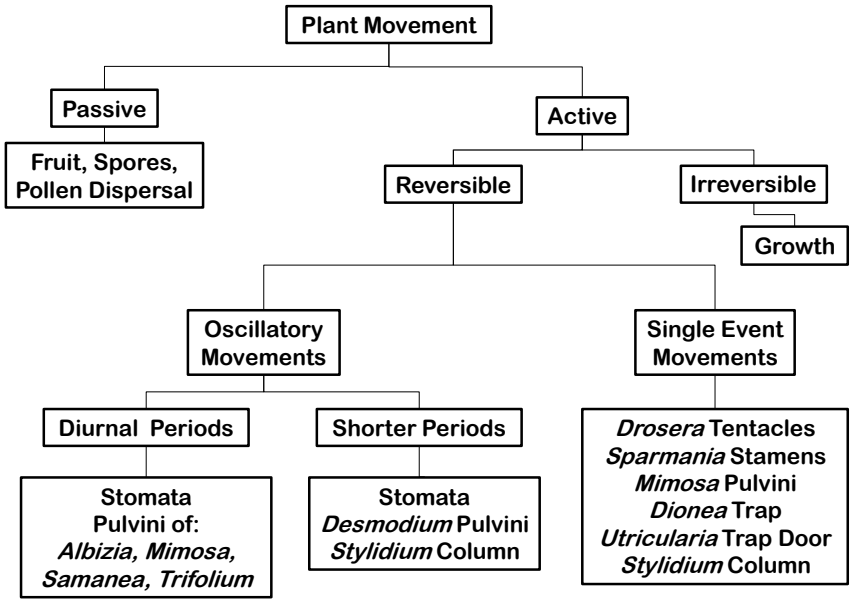

Figure 5. Hierarchy of the classification of plant movement with selected examples. The examples of single event movements discussed in greater detail are Dionea Trap and Mimosa Pulvini (Reproduced from Hill and Findlay [5]).

Burgert and Fratzl [6] present the actuation systems that enable plant movement. They organized movement into four mechanisms: cell growth, turgor pressure, cohesion

forces, and cell wall swell/shrink. Since turgor pressure is closest to the current study it is discussed in more detail. Turgor pressure uses a "motor cells" to create the driving force for actuation. Motor cells deform elastically when filled with internal pressure. Two plants, Dionaea muscipula (Venus flytrap) and Mimosa pudica (sensitive plant), with a whole organ that is actuated with turgor pressure are presented here. Dionaea muscipula is the fastest known plant movement at 100 ms for leaf closure during the initial rapid stage that results from drastic volume changes of the leaf cell/tissue. Mimosa pudica has motor cells on one side of the pulvinus, which is a flexible hinge at the base of the leaf. These motor cells rapidly lose their turgor pressure upon stimulation causing a reduction in bending stiffness of the hinge allowing the leaf to fold and droop. In Burgent and Fratzl's [6] synopsis feastures some recent research in the area. The paper builds a case that these actuation systems from nature could be used to create biomimetic, nature-inspired, actuating composites.

The Venus flytrap leaf is an example of a natural multifunctional material–the leaf structure–that has the ability to morph. Forterre et al [7] give a mechanical explanation for the rapid closure of the Venus flytrap (Dionaea Muscipula). The initial rapid closure, which takes about 100 ms, has an active biochemical component and a passive elastic component. An insect triggers closing by mechanically stimulating hairs. The leaf starts as a doubly-curved, i.e., curved in 2 orthogonal directions, leaf that is convex when open and then snaps to concave when closed. This snap-buckling closure starts out slowly; elastic energy is stored in the leaf over many hours as biochemical processes spring the trap. Closure is rapid when the leaf releases that energy. This morphing occurs more

rapidly than on-demand water movements can accomplish because of the quick release of elastic energy in the doubly curved leaf. A study of the trap closure dynamics shows what happens inside the tissue during closing. Fagerberg and Allain [8] presented their finding in the paper "A Quantitative Study of Tissue Dynamics During Closure in the Traps of Venus's Flytrap Dionaea Muscipula Elllis." They present the process in three distinct stages: closure, appresion, and sealing. These stages occur in the order listed. Closure stage is rapid flexure of the trap margins and curvature of the trap's lobes toward each other. This stage is complete by about 1 second after the trigger hairs are stimulated. Next the traps become noticeably more concave and the trap margins come into contact during appresion, which goes for about 30 minutes after the trap was stimulation. During the final stage, sealing, the margins become tightly appressed and the lower region becomes more concave and a water tight chamber is formed. The shape change at each stage is attributed to changes in volume of different regions.

Fagerberg and Allain's study used traps that were fully open and had never been triggered. The plants were raised in a green house for 5-10 years before being moved to a chamber with controlled temperature and light. The traps selected were similar in size. The tissue of the trap fell into five unique tissue groups. These groups are the upper epidermis, upper cortex, medullary, lower cortex, and lower epidermis. The upper epidermis faces skyward when the trap is open and becomes the inner surface after the trap sloses. The upper epidermis acts as a stomach lining during digestion. They analyzed the middle one-third of the trap, which they divided into three regions from the back–or mid rib–to the leading edge–or margin–of the trap.

They described the volume changes with a nondimensionalized parameter called the Relative Importance. This was done so different-sized traps and different tissue groups could be compared directly. The dynamics of tissue morphing and the tissue volume change responsible for closure in each stage was different. In the capture phase, the rapid movement to a concave shape that bends inward comes from the medullary and cortical tissue enlarging near the trap's free edge. The tissue that increased volume the greatest was the lower cortical, which is the major contributor to inward curvature. This expansion was mostly normal to the trap's midrib.

In the apression stage, the most significant tissues and region are the lower epidermal and cortical located in the third closet to the midrib–the back of the trap. Expansions in these tissues lead to further convexity. Finally, the sealing stage is mainly a consequence of tissue expansion in the lower epidermal tissue near the trap's edge and in the lower cortical and epidermal tissue in the traps's central region. The Venus flytrap demonstrates natural structural morphing through internal pressurization. This morphing occurs more rapidly than possible if only the water movements that control the anisotropic curvature changes could accomplish because the elastic energy stored buckling the doubly curved leaf is released quickly.

The Mimosa pudica is another example with rapid plant movement achieved by changing turgor pressure in specific cells. Allen[9] studied this seismonastic movement . His research goal was to explain the turgor pressure loss that occurs in the lower side of the pulvinus. This rapid plant movement, which is initiated by external stimuli, occurs in the lower side of the pulvinus at the base of the petiole, or leaf stock, in 1-2 seconds.

Allen[9] proposed that the pulvinar reactivity might be determined by the difference in turgor pressure or K^+ or Cl^- ion concentration differences between upper and lower pulvinar. He hypothesized the effect not directly related to absolute concentrations of K^+ or Cl^- ion.

Another attribute of the Mimosa pudica that inspires biomimetic structure design is the structural and functional properties of its folding geometry. Patil and Vaijapukar[10] studied this geometry to inspire new concepts for creating more efficient and optimum engineering structures through using innovative folding.

Copying nature in engineered objects is called as biomimetics. On this subject Bar-Cohen[11] wrote an overview. He discusses how nature has long functioned to initiate and motivate human innovation, and how replication of biological systems will continue to become more possible as science progresses. Nemat-Nasser et al[12] give human skin as an example of a multifunctional material that can heal, sense, protect, and provide structure simultaneously. Human bones present multifunctionality–they serve as structural support and as a manufacturing plant for blood cells. Meyers et al[13] give sea spicules; the abalone shell; the conch shell; toucan and hornbill beaks; and the sheep grab exoskeleton as five biological material examples that are highly-structured and multifunctional composites. Srinivasan et al[14] also discusses biomimetics and give three key characteristics of materials that can inspire design. These characteristics are multifunctionality, hierarchical organization, and adaptability. Multifunctionality is present in a tree root that acts as anchoring structure and as a conduit for nutrients. The tendon, with its intricate arrangement of material at different scales, illustrates

hierarchical organization. Adaptability is found in bones, with their ability to remodel to accommodate changes in load. Shrinivasan et al[14] also give four examples of composites (wood, insect cuticle, bone, and mollusk shells) found in nature that can spur ideas and development of new and novel synthetic multifunctional materials.

2.1.2 Synthetic Multifunctional Materials

Synthetic multifunctional materials can perform more than one beneficial function. Some synthetic multifunctional materials provide structure and sensing capabilities. Lin and Sodano[15] created an active fiber-reinforced composite by coating structural fibers a piezoceramic and embedding them in a polymer matrix. Curtis[16] built composite materials with damage detection and damage location abilities by incorporating fiber optics into the material. This material is called Smart Structural Health Monitoring System. Another concept, presented by Seepersad et al[17], is honeycomb materials designed to provide structure and tailored heat transfer characteristics for cooling.

Kumar and McDowell[18] have done work similar to Seepersad et al[17]. They studied how the mesostructure of two dimensional cellular structures can be tailored to achieve combine heat transfer and structural response optimally. This is done by varying the honeycomb's cell size, wall thickness, and cell topology.

Christodoulou and Venables[4] discuss four categories of multifunctional materials. Structural power materials systems are multifunctional materials that provide structure and act as a power source. They give four examples. The first is unmanned air vehicle powerfoils, which are a battery shaped like an airfoil. The next example is

powerfiber systems where the fiber batteries are embedded in the matrix and integrated into the reinforcing architecture as a rechargeable power source. Another is autophagous or self-consuming systems, which use the stress supporting structure as a fuel source. This is possible because, as the fuel is consumed, the structure weight decreases reduces the strength requirements. There are also four examples of autonomous sensing and actuating systems. Multifunctional electro-elastomers, which undergo extraordinary strains under applied voltage, are one illustration. Another instance is statically determinant structures called mechanotronics that, with a small number of deliberately placed actuators, can be flexed internally. Tensegrity structures are noted next. These structures are stiff bars connected by tensile elements that create an excellent shape-adaptive structure. The final example is machine-augmented composites–composite structures with simple machines incorporated for added functionality.

Structural materials that also serve as antennas comprise the electromagnetic multifunctional material systems. Survivable, damage-tolerant material systems are the last category and include both laminated multifunctional materials, which can contain a wide array of features, and autogenous or self-healing multifunctional materials. These self-healing materials usually arrest crack propagation with a thermoset matrix distributed in distinct phase regions. The common attribute throughout these examples is that they provide structure; the categories arise from the secondary function they perform.

Giurgiutiu et al[19] designed a synthetic nastic structure with embedded cylindrical microactuators in a polymer matrix. They sought to optimize the design variables that

described both the nastic material properties and geometry. Their optimization criterion was maximum actuation distance for a fixed actuation fluid volume. The actuation distance is a function of 8 master variables. They also built a case for the potential of synthetic nastic structures as high energy density materials by replicating nautral nastic structures. They want to mimic plants capable of localized-movement nastic motion that occurs in specialized motor cells. In this material biochemical reactions create cell volume changes, caused by water traveling in and out of these motor cells, that lead to overall tissue deformation. The changes in volume are not uniform and therefore cause deflection rather than overall uniform expansion. These motor cells that exhibit nastic motion in plants are a natural hydraulic actuator.

2.2 Shape Changing and Morphing Materials

A special class of synthetic multifunctional materials related to this study is shape changing and morphing materials. To change shape must be a way to apply the force and displacement necessary to do the work the shape change requires. These materials will be discussed based on their actuation method. The actuation methods are piezoelectric, shape memory alloys, and pneumatic. Hyer and Jilani[20] created a rectangular, unsymmetric, laminated piezoceramic material, and tried to predict its behavior. Hassan[21] developed shape-memory alloy, chiral-honeycomb cells that, when grouped together, make up a truss structures. Their objective was making a functional material that increases in volume. Hirai et al[22] built pneumatic actuators composed of multiple elastic tubes that can achieve multiple motions by implementing various

pressurization schemes. The present work is an outgrowth of prior research with machine augmented composites.

2.3 Machine-Augmented Composites

Machine augmented composites incorporate small, simple machines in a matrix to achieve multifunctionality. Embedding small hourglass-shaped systems in a matrix material has previously been investigated by McCutcheon[1], McCutcheon et al[23], and Kim[24] McCutcheon's work looked at the possibility of creating a material with high damping by using the embedded hourglass as a passive structure that dissipates energy by moving a viscous fluid. Kim[24] also used MHAs as a passive damping system; however, he looked at increasing the damping of a composite material while maintaining its stiffness. The primary effect in damping was the additional free, highly sheared surfaces the hourglass shaped machines introduced. He also used a viscous fluid in the hourglass to increase energy dissipation. Compared to the work of Kim and McCutcheon, the contribution from the present work with MHAs is that this work considers the materials for active actuation, not for passive damping. Tang et al[25] incorporated a small four-bar linkage machine into a polyurethane matrix to create a machine augmented composite that converts a compressive load into shear. An active machine-augmented composite is one possible application for the miniature hourglass shaped actuators investigated in this study.

2.4 Morphing Wings

The morphing wing concept and the multiple ideas aabout how they might be designed, is of special interest to this research because that is the projects ultimate goal.

Morphing wings powered by internal pressure are discussed here. Active, pressurized MHAs might help achieve this goal.

There are many ideas for creating a morphing wing structure. Thill et al[26] summarizes the concepts and ideas related to morphing wings that deal specifically with smooth and continuous morphing structures. These structures deform while carrying load. They cover concepts for wings structures that are stiff in the span, yet flexible in the chord direction. Thill et al[26] groups the concepts into four categories. These categories are change in surface area, change in shape that is due to stiffness tailoring, change in shape that is due to stiffness change, and other mechanical morphing concepts.

The surface-area-change concepts include stretchable structures. Elastomers and auxetic, i.e., negative poisson's ratio, materials exemplify this concept. Deployable structures are surface-area-change structures. The example deployable structures are rollable/collapsible structures, foldable structures, inflatable structures, and overlapping/stacked/nested structures.

The stiffness tailoring approach is presented with five examples. These examples are extreme anisotropic materials, multi-stable composites, segmented structures, folded inner skin structures, and multilayered skin structures. Shape memory materials--including shape memory alloys, shape memory polymers, elastic memory composites, shape memory textiles, and magnetic shape memory materials—are one illustration of shape change enabled by stiffness tailoring. Another concept in this category is flexible matrix composites.

The final group referred to as morphing concepts is a broader category that includes mechanical ideas like the finger concept, belt rib concept, sliding rib/crossbar concept, eccentuator, and compliant structure. They are many concepts for morphing wing structures. Baker and Friswell[27] propose a wing structure completely made from determinant truss members with some of the members replaced with actuators to deflect the structure without stressing other members. Inoyama et al[28] explored distributing actuators throughout a wing structure to optimize actuator placement to achieve a morphing wing. There much work currently on creating a wing structure that continuously and smoothly transitions from an undeformed to a deformed configuration.

The idea of using pneumatic pressure to create a morphing wing is not new. There is class of inflatable morphing wings. Cadogen[29] discusses inflatable wings for unmanned aerial vehicles. Inflatable wings are studied because they can be deployed from a stowed volume that is much smaller than the working volume. Once deployed, the wing's performance might be increased by morphing them. The morphing wing would improve aerodynamics and eliminate mechanical actuation systems. Cadogen's[29] idea requires small embedded actuators. The options listed are piezoelectric, electro-active polymers, shape memory alloys, pneumatic chambers, nastic cells, and distributed motor-actuator assemblies. Cadogan discusses three ideas for overcoming the major challenge of morphing a conventional rigid structure that must be stiff inherently. These ideas are nastic structures, bump flatting, and trailing edge deflection. In the nastic structures concept the morphing is caused by the inflation of cylindrical tubes that are lie on the wings lower surface and are aligned parallel to the length of the wing. This

inflation reduces the wing's bottom surface length thus causing it to bend downward. This concept is a possible use for miniature hourglass shaped actuators.

The work done by Yokozeki et al[30] is a possible way to implement the miniature hourglass-shaped actuators. Yokozeki et al proposed corrugated composites for candidate for flexible wing structures. These are very flexible in the corrugated direction, which becomes the chord direction for the wing, but stiff in the perpendicular direction, which is the wing's span. These corrugated composites exhibit ultra-anisotropic sitffness. A possible use for the MHA is that a MHAs could be placed in the corrugations. This would allow the material to flex depending on how the MHAs were pressurized. Pressurization of the MHAs on the top would cause the corrugated material to curve downwards; likewise, pressurization of lower MHAs would bend the structure upward. Pressurizing both top and bottom simultaneously would extend the chord and stiffen the structure. A schematic corrugated composite material appears in Figure 6.

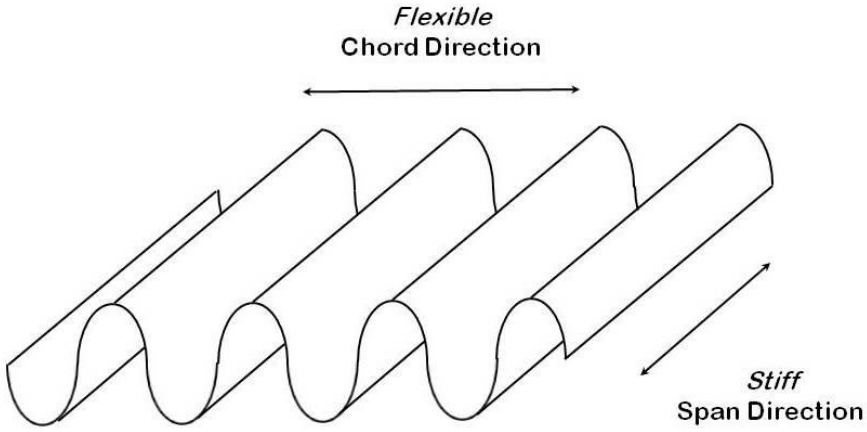

Figure 6. Illustration of a corrugate composite material. Corrugated composite material offer a possible platform where MHAs could be implemented. (Recreated from Yokoseki et al[30]).

Leung and Guest[31] investigated the placement of one linear actuator in an infinite kagome lattice. The kagome lattice structure has potential for active truss structures that integrate linear actuators into the structure. These kagome lattice structures, whose response depends substantially on the initial geometry, have high passive stiffness and low actuation resistance, which makes them a strong candidate for active structures. An MHA could be the linear actuator incorporated in the lattice. Figure 7 below shows a kegome lattice with one member circled where an actuator could be placed. There is the possibility that linear actuators could replace many members in the structure to create a structure that undergoes a complex deformation.

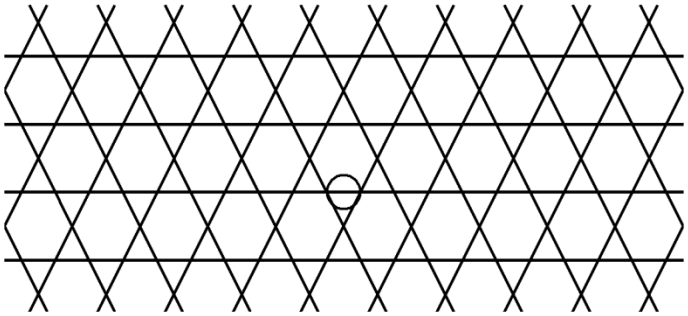

Figure 7. Illustration of a kagome lattice structure with single truss member for possible actuator replacement circled. MHAs could replace truss members in a kagome lattice structure in a manner that creates a desired deformation when the MHAs are pressurized and elongate.

Similar to the work described previously with kagome lattices Inoyama et al[28] performed topology synthesis of distributed actuation systems for morphing wing structures. They used the uniform truss structure shown below in Figure 8. Then they developed an optimization process that takes a desired deformation and decides which

structural member should be one of the five types they use. The five types of members are inactive telescope, active telescope, actuator, frame, truss, and, void. An inactive telescope can support a moment and shear force but cannot support an axial force. An active telescope also supports a moment and shear force but it can supply an axial extension or contraction force. Third type of member is an actuator that supplies an axial extension or contraction force but cannot support a shear force or bending moment. Next is the frame member which can support all three: bending moment, shear force, and axial force. The truss member can only support an axial force. A void, the last type of member, which as its name suggest cannot support any load.

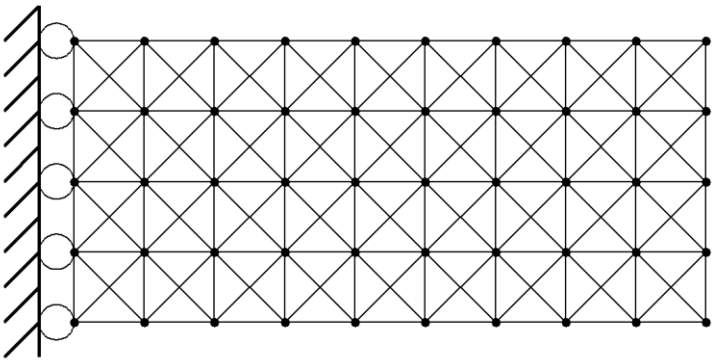

Figure 8. Illustration of a truss structure for member placement optimization. The truss members can be any of the five types which are inactive telescope, active telescope, actuator, frame, truss, and, void. In this truss structure the actuator member could be a MHA. (Recreated from Inoyama et al[28]).

There are many possible applications were MHAs could be incorporated into a structure. MHAs could be integrated into any design where a miniature linear actuator is applicable such as corrugated composite materials, determinate truss structures, and

kagome lattices. These actuators could likely be used in parallel with extreme anisotropic materials.

The present study considers one possible actuator. This study is not a comprehensive analysis of a morphing wing; it is an inquiry into the MHA response. The question considered is “what are the tradeoffs associated with MHA performance within a design envelope defined by maximum possible deflection, mechanical advantage, and available work density. This makes the current study different from other work on morphing structures that investigate the entire structure without looking at the actuator separately.

3. FINITE ELEMENT CODE: A COMPLETE SELF-CONTAINED CODE FOR SPECIALIZED SIMULATION

The finite element code used to conduct this study runs in MatLab. It is a complete, self-contained code written for one purpose: model the MHA's deformation under an internal pressure. It contains the main program and many sub routines. These sub routines include a mesh generator, functions that create force and stiffness matrices, and boundary conditions. Each of these subroutines are discussed in detail.

3.1 Code Operation

The program's main section accepts the user's input. This includes the parameters that describe the MHA geometry, the material properties, the mesh information, and control inputs for running the simulation. In the main section the global equations are built and solved. The main program calls several function, sends them variables and parameters, and collects the calculated information. This occurs for each for each load step and iteration. The main section's code appears in Appendix A.

The first functions is "PressureSide," which uses the element mesh information to create an array that states what elements have pressure applied to them and to what side it is applied. Appendix B contains this code.

The second function is "MHA_MESH_GENERATOR", which has its full code in Appendix C. This code is the mesh generator. This mesh generator is written for the MHA geometry specifically. It uses the input parameters that define the MHA geometry, places the nodes, and builds a mesh. The mesh generator also creates some important arrays used throughout the simulation. It creates a nodal connectivity array that states

what elements and local node numbers correspond to what global nodes. The degree of freedom connectivity array is similar to the nodal connectivity array and contains information on what global degree of freedom corresponds to what element and local node. The mesh generator also produces the total number of nodes, the number of elements, and an array containing both the x and y nodal coordinates. Finally, the mesh generator constructs four arrays that contain the global node numbers of nodes that lie on the MHA bottom surface, the MHA inner surface, the axis of x symmetry and the axis of y symmetry. Only one quadrant of the MHA is analyzed–there is axial symmetry in x and y directions. An example computational domain mesh appears in Figure 9.

The next two functions called deal with creating boundary conditions. The first, named "BoundaryConditions," which is presented Appendix D, uses the mesh generator's information about the nodes that lie on the MHA bottom surface and on the x and y axes of symmetry. It uses this information to create an array that contains all the global degrees of freedom that have applied boundary conditions and to create an array that contains those boundary conditions that are all initially set to zero. The boundary conditions that enforce symmetry remain at zero throughout the simulation. The second function, "SteppedBottomDisplacementBC", creates an array containing the degrees of freedom along the bottom surface that will cause stepped displacement and an array containing values of those degrees of freedom. Initially set to zero, these values will change at each displacement step. The arrays created by this function will copied at each displacement step into the arrays created previously. This code is in Appendix E.

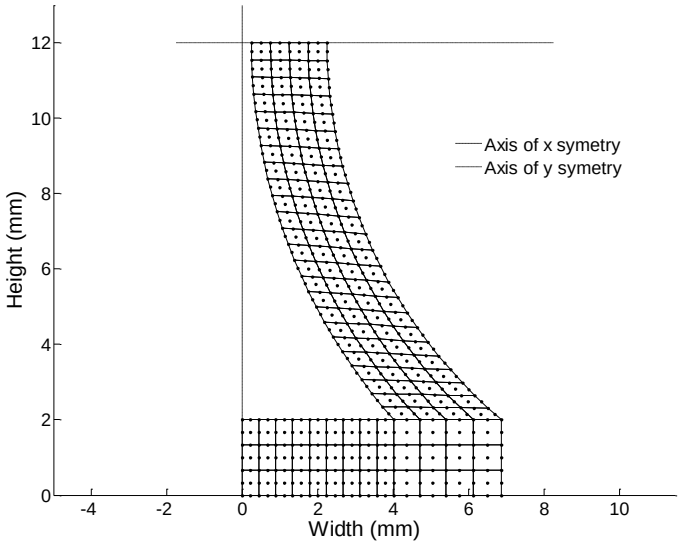

Figure 9. Mesh of the MHA computational domain. Only one quadrant is meshed and used with symmetry boundary conditions to compute the MHA behavior. The bottom right quadrant is shown with both the x and y axes of symmetry.

Presented in Appendix F, "ElementStiffness4UpdatedLagragian" is the next function called by the main program. This function creates the element stiffness matrices. It uses either the plane-stress or plane-strain assumption to create the element stiffness matrices. This function can use nine node quadratic elements only. "ElementForce4UpdatedLagragian," which creates element force vectors, is the next function. It appears in Appendix G. This element force function uses a function presented in Appendix H, "MHA_Pressure," that calculates the forces on each nodes that subjected to the internal pressure. It calculates the magnitude and direction of forces from pressure using the nodal coordinates that describe the surface. Both the element force and stiffness functions use the interpolation function, which uses a function that

contains the gauss point weights and coordinates, for numerical integration. These functions appear in Appendix I and Appendix J respectively.

The function "MHA_Work" uses the MHA simulation results to calculate mechanical advantage, work advantage, percent elongation, MHA work density, and work density of a traditional actuator. This function, which uses the code from "MHA_Force" (Appendix K) that calculated the force on the MHA bottom, is contained in Appendix L. Appendix M lists the final function, "MHA_FULL_COORDINATES" called by the main program. This function creates arrays that contain the nodal coordinates necessary to define the undeformed and deformed MHA nodes. These nodes can be plotted if necessary.

The finite element simulation uses nine-node quadratic elements. These elements use the same interpolation functions to interpolate both the primary variables and the geometry so they are isoparametric elements. This is described in Reddy[32]. The element type used to simulate the MHA deformation are solid continua elements. The formulation used is the updated Lagrangian from Reddy[33]. The book by Cook[34] and unpublished notes of Dr. Alan Palazzolo[35] provided to the graduate course MEMA 647-Theory of Finite Element Analysis during the summer of 2007, were referred to extensively in writing the MHA simulation code. The full three dimensional case is reduced to a two dimensional simulation by assuming plane-strain. This can be done because the MHA is sufficiently long in the out of plane direction, which is normal to the MHA cross section. In addition, there is no load that would create out-of-plane strain. This plane-strain assumption does not investigate what happens near the ends of

the MHA. It neglects any edge effect where the MHA is sealed. The MHA must be sealed to contain 5 MPa internal pressure; however this is done, it would create some end effects that are not captured by the plane-strain model.

The internal pressure is applied normal to the MHA inner surface and as the MHA deforms the software recalculates the normal direction at every iteration and load step. The unit normal vector is calculated from the nodal coordinates according to the work of Gregory S. Payette[36]. Although this work follows the unpublished work of Payette, there are published articles on applying pressure boundary conditions on moving boundaries. These include the work Schweizerhof and Ramm[37] and Simo et al[38].

To validate the finite element code, a study was performed that compared the analytical results from a fixed-fixed Euler-Bernoulli beam to the new finite element code results. To check the finite element code the deflection of a straight MHA side-wall was compared with an Euler-Bernoulli beam with the same geometry. The MHA side-wall was made straight by giving it a very large radius r equal to 2540 m (100,000 inches) and a small arc angle α equal to $\pi/10{,}000$. This yields a beam length equal to 798 mm (31.42 inch). Symmetry makes the computational domain only one half the original length. The beam thickness and depth are both 25.4 mm (1 in.) making the second moment of area about the neutral axis of the beam equal 3.47 cm^4 (1/12 $inch^4$).

The boundary conditions at the end section are completely constrained. There is symmetry corresponding to the beam center. In addition, the two nodes that are at the edges of the side-wall base have both degrees of freedom set to zero. These boundary conditions create a fixed-fixed beam. The load is a uniform pressure. This load and

boundary conditions create the "Fixed supports - uniform load" beam configuration shown in Table A-9 of Shigley[39]. The simulation results were compared to the relation for the maximum deflection given by Shigley is given in the equation (3)

$$y_{max} = -\frac{wl^4}{384EI} \tag{3}$$

The beam receives a uniformly distributed load of 43.8 N/mm (250 lbs per inch). The beam's material properties are similar to steel with a 207 GPa (30 Mpsi) Young's modulus and a 0.25 Poisson's ratio. The beam simulation ran with the beam made into a two-dimensional plane-stress problem. The beam validation mesh appears in Figure 10.

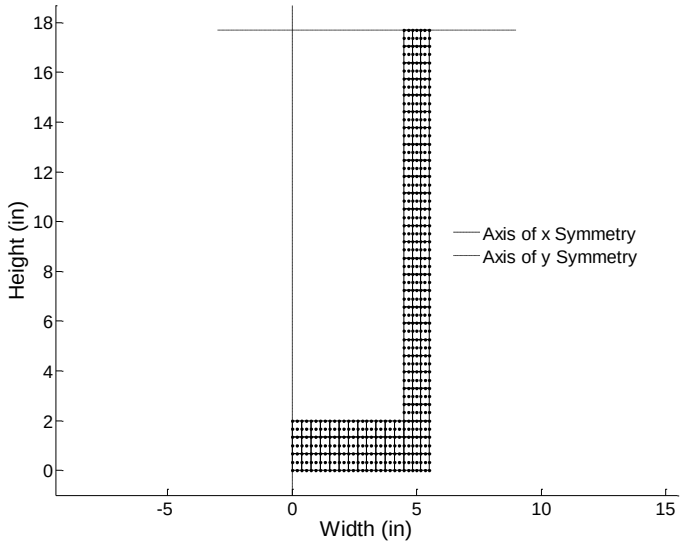

Figure 10. Mesh of quadrant used as the computational domain for code validation. The analysis code was validated for a fixed-fixed beam. The mesh is one half of the beam with a symmetry boundary condition in the middle and is fixed at the other end. This geometry is created by making the arc radius very large and the arc angle very small.

The results support the code's validity. For a mesh with 24 elements along the length, 3 elements through the cross section, the finite element code results gave an 6.393 mm (0.2517 inch). which is 0.78% less than the Euler-Bernoulli results that predicted a 6.444 mm (0.2537 inch) maximum deflection. These results are close and it is reasonable to believe that the Euler-Bernoulli result would predict a higher deflection because it does not account for any geometric, nonlinear stiffing effects. The results for the deformed and undeformed geometries appear in Figure 11. The deflections are relatively small compared to the deflections that the MHA will undergo, but, because the linear Euler-Bernoulli results would not be accurate for large deflections, they were compared with a small defection problem. This validation study provides evidence that the finite element code is working and yields reasonable results.

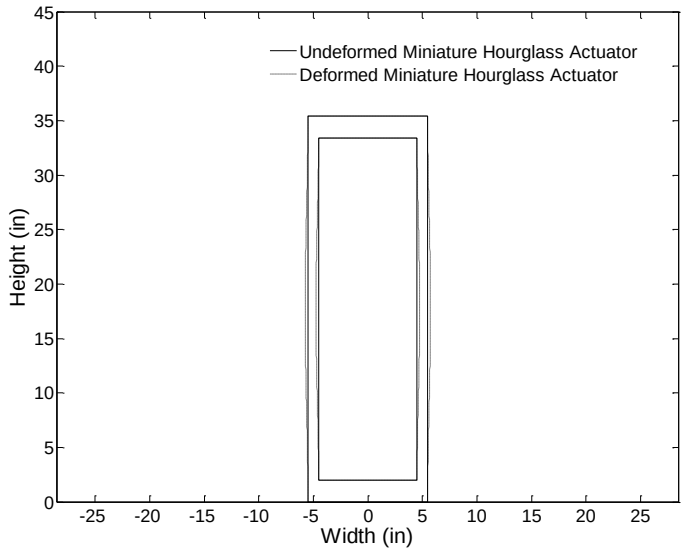

Figure 11. Illustration of the validation beam before and after deformation. The whole MHA with straight side-walls is plotted but only one quadrant is used for the computation. The code result was only compared to Euler-Bernoulli beam solution for this small deflection.

3.2 Mesh Refinement Study

A mesh refinement study was done to make sure that the results were not significantly affected by the number of degrees of freedom. Five meshes were studied starting with an 8x1, which is 8 elements along the beam and 1 element through the beam, that was repeatedly refined to 40x5. The results for the maximum deflection for these two meshes are 6.210 mm 0.2445 inches and 6.421 mm 0.2528 inches, respectively. This is only 3.4% difference between the coarse and a significantly more refined mesh. Only 0.16% difference was seen between the last refinement and the previous one. The full mesh refinement results appear in Table 1.

Table 1. Summary of mesh refinement results in beam validation study. There is only a 3.4% difference between the finest and coarsest meshes and only 0.16% between the last two mesh refinements.

# of Elements Along the Beam	# of Elements Through the Beam	Δ_{max} mm (in)
8	1	6.210 (0.2445)
16	2	6.358 (0.2503)
24	3	6.393 (0.2517)
32	4	6.411 (0.2524)
40	5	6.421 (0.2528)

These results are evidence that the simulation outcome is not significantly dependant on the size of the mesh. This is true because the results agree within an acceptable error level even when very different mesh sizes are used.

4. MINIATURE HOURGLASS SHAPED ACTUATOR CASE STUDIES: EFFECT OF GEOMETRY CHANGES

Three distinct cases are examined. The first, Case 1, looks at the effects of changing the MHA side-wall geometry while holding the MHA height constant. For Case 2, the arc length of the MHA side-wall is held constant while the shape is altered. In Case 3, the MHA geometry with the highest work density from Case 1 and Case 2 is used. The side-wall shape is held constant while its thickness is changed. For each sample geometry within the three cases, a finite element simulation was performed to investigate the mechanical advantage, work advantage, percent elongation and work density are investigated and reported.

After creating the MHA specific finite element mesh, the MHA simulation process begins with filling the MHA to an internal pressure of 5 MPa in five 1 MPa load steps while the ends of the MHA are constrained so that no expansion is allowed. These load steps are done to allow the solution to converge with less iteration, which makes the code run faster. At this point, the forces on all the nodes that lie on the MHA computational domain's bottom surface are summed and saved. This is the blocked force and the information needed to calculate mechanical advantage. The constraints are then removed and internal pressure causes the MHA to extend in two ways. First, the internal pressure acts on the top and bottom of the MHA causing it to extend along its height from the pressure acting in extension direction. Second, the internal pressure bends the MHA's side-walls. As the side-walls straighten, they push the top and bottom of the MHA. This increases the force beyond that from direct pressure alone. This increase is

called the mechanical advantage. Next, the MHA computational domain is allowed to expand in 0.02 mm steps, which corresponds to the full MHA expanding 0.04 mm. At each increment, the program checks whether the MHA side-wall begins to buckle out. If this happens, the side-wall deflection no longer aids in the axial expansion, thereby hindering the MHA performance and rendering further simulation unnecessary. At this point, the simulation stops and saves the results from the previous expansion step—when the MHA side-wall was not buckled outward. For each displacement step, the forces on the MHA ends are computed and saved so that work can be calculated. The work density per unit length of the MHA is calculated by dividing the total work performed by the initial cross sectional area. The percent elongation is the MHA height at the last displacement step when the MHA side-walls are not buckled compared to the initial height. The work advantage is the total work performed divided by the work of a comparable traditional actuator. The following is a discussion of the simulation results for each case study.

4.1 Case 1. Constant MHA Height

In Case 1 the side-wall geometry changes because the arc angle, α and the arc radius, r, change. The MHA height stays constant because the product of the arc radius and the sine of half the arc angle is constant. This relationship is contained in the equation (4)

$$r\sin\left(\alpha/2\right)=10 \tag{4}$$

The arc angle α is the primary parameter that is varied and the arc radius r is then chosen to keep the MHA height constant at 24.0 mm. The interior height is 20 mm with the top,

bottom, and the side-walls each have a thickness of 2 mm. The arc angle and arc radius for each of the geometries in Case1 are in Table 2.

Table 2. Arc angle, α and arc radius, r for Case 1 geometries. The arc angle is stepped by π/32 and the arc radius is calculated to keep the MHA height constant.

α	$\frac{11\pi}{32}$	$\frac{12\pi}{32}$	$\frac{13\pi}{32}$	$\frac{14\pi}{32}$	$\frac{15\pi}{32}$	$\frac{16\pi}{32}$	$\frac{17\pi}{32}$	$\frac{18\pi}{32}$	$\frac{19\pi}{32}$	$\frac{20\pi}{32}$	$\frac{21\pi}{32}$
r	19.45	18.00	16.79	15.76	14.89	14.14	13.50	12.94	12.45	12.03	11.66

These arc angles were chosen because they go from a side-wall that is almost straight at $\alpha=11\pi/32$ to a side-wall that is nearly a half circle at $\alpha=21\pi/32$ in 12 steps. Between these two extremes are the geometries of interest.

4.1.1 Case 1. Constant MHA Height Maximum Mechanical Advantage

The Case 1 MHA geometry, shown in Figure 12, that exhibits the highest mechanical advantage is $\alpha=11\pi/32$ and r=19.45 mm. These parameters yield side-walls that are straighter than any other Case 1 geometry. The mechanical advantage results in a significantly large value of 6.47. This MHA high mechanical advantage happens because the shape of the MHA transfers some of the load to the ends. However, the total elongation for this case is small therefore making this geometry is unlikely to be useful except possibly in applications where large force and a very small displacement are needed. The work density is also determined to be a low value of 0.113 MJ/m^3. Even though the force is high, the elongation is too small to achieve a significant work density. Even though the side-wall deformation is noticeable the elongation of the MHA is very small.

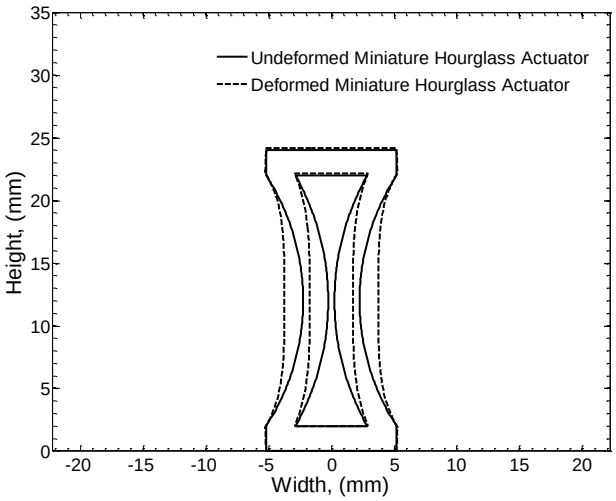

Figure 12. When the MHA has the shape shown with $\alpha=11\pi/32$ and r=19.45 mm, the MHA produces the maximum mechanical advantage in Case 1. The dashed lines show the MHA's free displacement at 5 MPa internal pressure. The elongation is very small at only 0.67% of the MHA height.

Figure 13 shows that the force stays high through the entire elongation of the MHA because the elongation is small. The total elongation was only four steps reaching an elongation of 0.16 mm or 0.67% of the MHA Height. The reason that the elongation stops long before the force goes to zero is that the side-walls start to buckle out. Despite the force per unit length remaining above 160 N/mm, this geometry would probably not be useful because of its small elongation. The total work density the MHA can perform is 0.113 MJ/m^3. The comparable traditional actuator can only achieve a work density of 0.018 MJ/m^3 because the elongation and force are both small.

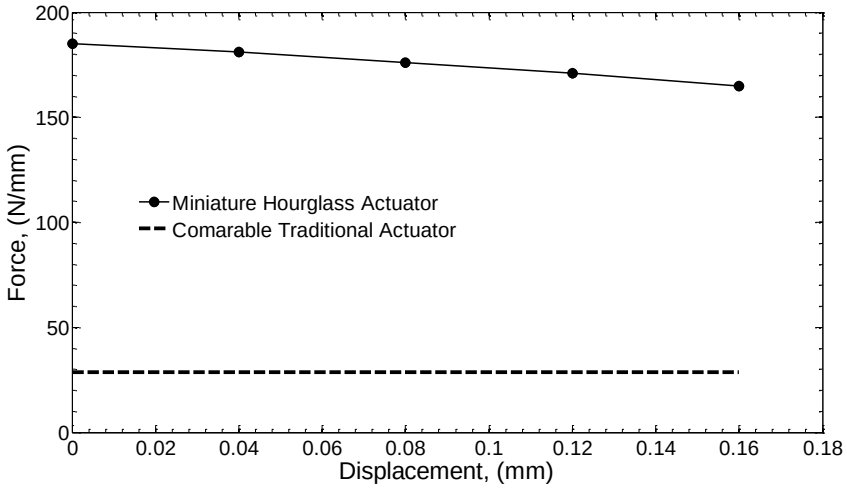

Figure 13. Force supplied by the MHA and CTA verse actuator displacement. This chart shows that a conventional actuator has a constant force through the MHA's displacement range. The best Case 1 MHA always has a larger force; however, the force drops 11 % with displacement.

4.1.2 Case 1. Constant MHA Height Maximum Percent Elongation

The maximum percent elongation in Case 1, 8.67%, happened to be the highest percent elongation of any case studied. This MHA has an arc angle and radius of $\alpha=21\pi/32$ and r=11.66 mm respectively which also gives it a 24.0 mm side-wall arc length, the longest of any MHA geometry. The geometry with and without deformation is presented in Figure 14. It should be noted this figure is actually a couple of displacement steps before the code stopped from side-wall buckling because the load went to zero before the side-walls buckled. This is not obvious by looking at Figure 14.

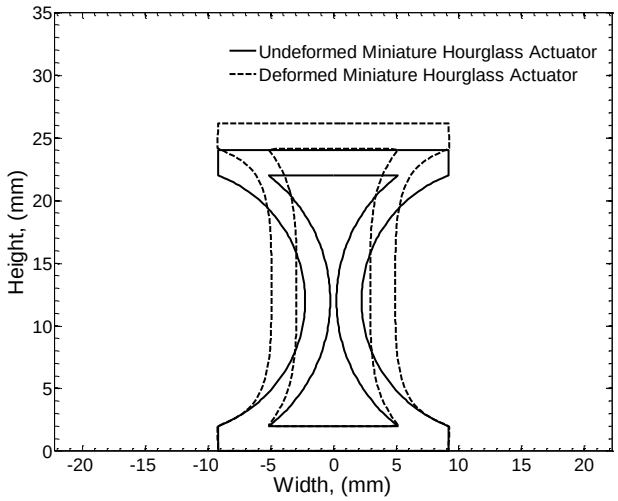

Figure 14. This Case 1 geometry, of $\alpha=21\pi/32$ and r=11.66 mm, has the highest elongation percentage. This geometry produces an elongation of 2.08 mm which is 8.67% of the MHA height when pressurized to 5MPa.

Figure 15 displays how near the end of the elongation the force approaches zero which is expected for a MHA with high elongation. At high elongation all the force on the MHA internal top and bottom faces is balanced by force from the side-walls trying to spring back. This happens before the side-walls start to buckle out. The work density for this MHA is only slightly less than the maximum at 0.389 MJ/m^2. Up until displacements greater than 1.65 mm, the force output is higher than the force supplied the comparable traditional actuator.

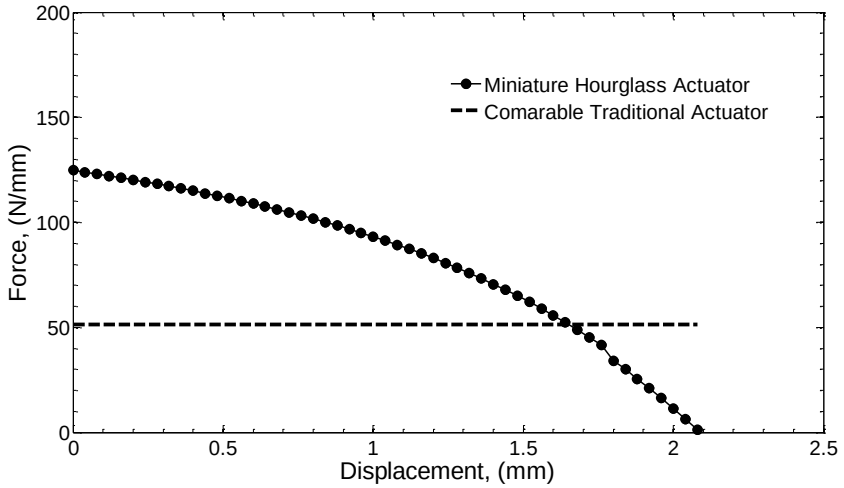

Figure 15. This force versus MHA displacement for the Case 1 geometry with the highest elongation shows a decline that almost reaches zero as the MHA gets fully extended. High elongation limits the MHA's force because the force drops rapidly as the hourglass extends.

4.1.3 Case 1. Constant MHA Height Maximum Work Density

In Case 1, the MHA geometry that achieved the highest work density had an arc radius and angle of r=12.94 mm and $\alpha=18\pi/32$ respectively. This geometry lies between the geometries of highest mechanical advantage and highest percent elongation which is expected because the ability to do work requires applying a force over a distance. The blocked force per unit length is 135 N/mm and the elongation is 0.67% or 1.60 mm. The geometry of this MHA along with the deformed geometry is illustrated in Figure 16, while the force versus displacement behavior is shown in Figure 17.

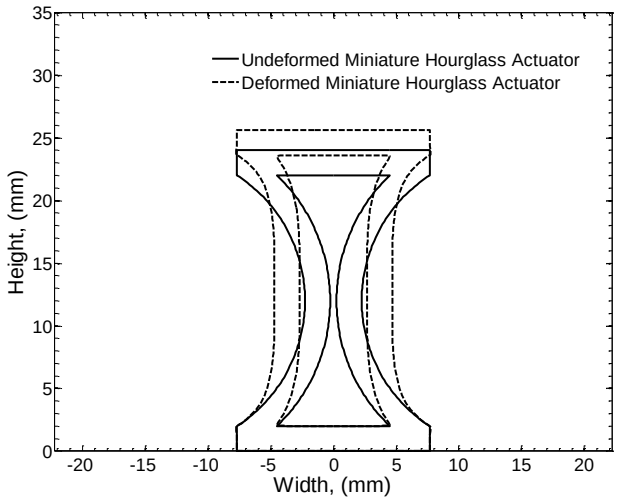

Figure 16. The Case 1 MHA with the maximum work density has an arc angle between the maximum force and maximum elongation shapes. This means that there is an optimum trade-off between force and displacement that generates the greatest possible work.

For this set of parameters a value 0.396 MJ/m^3 of work density was calculated, while the comparable traditional actuator only exhibited a work density of 0.195 MJ/m^3. Figure 17 shows that the force initially declines at a slower pace but then as the MHA expands and its sides get straighter the force begins to decline rapidly. At an elongation of 1.38 mm the force the MHA can exhibit falls below the force that the comparable traditional actuator can provide. Between a displacement of 1.44 mm and 1.48 mm the curve slope quickly gets steeper and then returns to the previous slope. The reason for this unknown but the simulation did reach a converged solution at every displacement step.

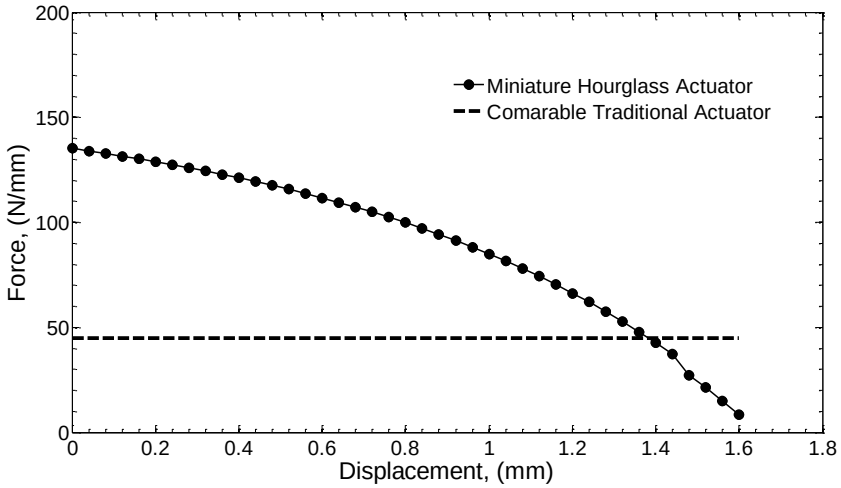

Figure 17. The Case 1 MHA with the best work density shows a force drop that is almost as large as the drop produced by the shape that obtains the greatest elongation.

4.1.4 Case 1 MHA Mechanical Advantage and Work Density

For the geometries in Case 1 the percent elongation shows an almost linear rise with increase in arc angle. This is likely due to the fact that as the arc angle increases the arc radius decreases, thereby increasing the side-wall curvature. This in turn makes it easier to straighten and allows the MHA to elongate. In addition, total the arc length increases from about 21 mm for the $\alpha=11\pi/32$ case to 24 mm for the $\alpha=21\pi/32$ geometry, which increases the potential maximum elongation. Both the force and work advantage fall with the increase in arc angle displaying nearly the same behavior but for a different reason. The mechanical advantage falls because the more curved side-walls do not add addition force to the MHA ends as much as straighter side-walls. In the case of the larger arc angle side-walls the side-wall acts as a supporting arch which does not transfer much of the load to separating the two MHA ends. The work advantage falls because the as the elongation increases the work density of the Comparable Traditional

Actuator rises faster than the MHA work density. The results of Case 1 are shown in Figure 18.

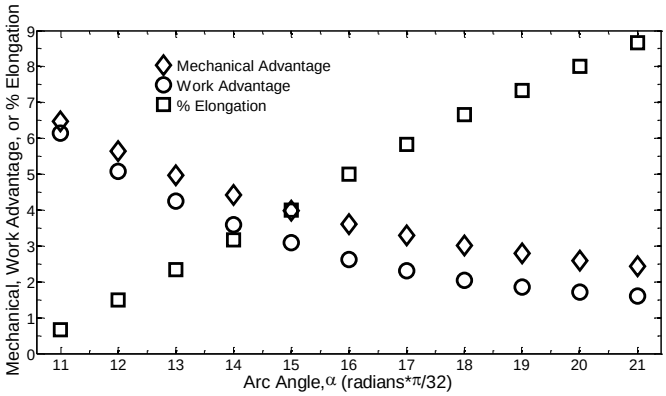

Figure 18. Force and work advantage along with % elongation plotted versus arc angle for a fixed MHA height. The Force and work advantage fall as the arc angle increases while the elongation increases.

When the MHA height is held constant the work density increases from a value of 0.113 MJ/m^3 when $\alpha=11\pi/32$ and r=19.45 mm to a maximum value of 0.396 MJ/m^3 when $\alpha=18\pi/32$ and r=12.94 mm. There is little difference in the work density from $\alpha=\pi/2$ to $\alpha=21\pi/32$ as can be seen in Figure 19. The work density of a comparable traditional actuator does change for every geometry case. This is because the main factor in its work density is the percent elongation. When comparing Figure 18 and Figure 19 it is clear that the percent elongation and the work density of a comparable traditional actuator increase following the same trend. These results are summarized in Table **3**.

The work density of a Comparable Traditional Actuator increases in a nearly linear fashion following the behavior of the MHA percent elongation increase. This happens because the CTA force is constant and equal to the force from pressure applied to the MHA top inner surface which is only a function of the MHA width based on the R

value assigned. This leads to a work increase that directly follows an increase in elongation. This is true for all MHA geometry cases.

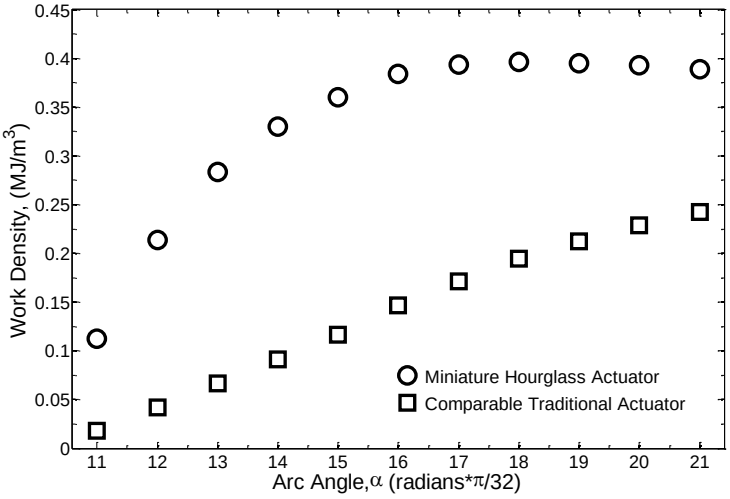

Figure 19. MHA and CTA work density plotted versus arc angle. When the MHA height is fixed, the work density rises to a maximum value at $\alpha=18\pi/32$. The Comparable Traditional Actuator does not achieve the work density found for the MHA at each arc angle.

Table 3. Results for Case 1 analysis covered arc angles from 11π/32 to 21π/32 and had a constant MHA height of 24.0 mm.

Arc Angle α	Blocked Force (N/mm)	Mechanical Advantage	Work Advantage	Elongation (mm)	% Elongation	Work Density (MJ/m^3)	Comparable Traditional Actuator Work Density (MJ/m^3)
11π/32	185	6.47	6.14	0.16	0.67	0.113	0.018
12π/32	175	5.64	5.07	0.36	1.50	0.214	0.042
13π/32	166	4.98	4.25	0.56	2.33	0.283	0.067
14π/32	158	4.43	3.60	0.76	3.17	0.330	0.092
15π/32	151	3.98	3.09	0.96	4.00	0.360	0.117
16π/32	145	3.60	2.62	1.20	5.00	0.384	0.146
17π/32	140	3.29	2.30	1.40	5.83	0.394	0.171
18π/32	135	3.02	2.03	1.60	6.67	0.396	0.195
19π/32	131	2.79	1.86	1.76	7.33	0.395	0.213
20π/32	128	2.60	1.72	1.92	8.00	0.393	0.229
21π/32	125	2.43	1.60	2.08	8.67	0.389	0.243

4.2 Case 2. Constant MHA Side-Wall Arc Length

This study was similar to Case 1 in that both the arc angle, α, and the arc radius, *r*, are varied. In this case, the product of the arc radius and the arc angle is held constant. This relationship is given in equation (5).

$$r\alpha = 20 \tag{5}$$

Holding the arc length constant at 20 mm allows the MHA height to vary from 23.0 mm for the geometry where $\alpha=11\pi/32$ to 20.6 mm where $\alpha=21\pi/32$. Table 4 below contains all the values of arc angles and arc radii for Case 2.

Table 4. Arc angle and arc Radius for Case 2 geometries. The arc angle is stepped by $\pi/32$ and the arc radius is calculated to keep the MHA side-wall arc length constant.

α	$\frac{11\pi}{32}$	$\frac{12\pi}{32}$	$\frac{13\pi}{32}$	$\frac{14\pi}{32}$	$\frac{15\pi}{32}$	$\frac{16\pi}{32}$	$\frac{17\pi}{32}$	$\frac{18\pi}{32}$	$\frac{19\pi}{32}$	$\frac{20\pi}{32}$	$\frac{21\pi}{32}$
r	18.52	16.98	15.67	14.55	13.58	12.73	11.98	11.32	10.72	10.19	9.70

4.2.1 Case 2. Constant MHA Side-Wall Arc Length Maximum Mechanical Advantage

As in the previous case, the maximum mechanical advantage is associated with a small total elongation of 0.28 mm which is only 1.22% of the MHA height. Even though this elongation is small it is significantly larger than the 0.16 mm seen in Case1. The reason that this Case 2 geometry could elongate more is that the arc length is 20.0 mm compared to the 21.0 mm in Case 1 which might be just enough difference to keep the side-wall from buckling out as early. As can be seen in Figure 20 this elongation is still very small. Interestingly the work density in this geometry is 0.173 MJ/m^3 which is only

13% lower than the 0.199 MJ/m^3 for the Case 2 geometry with the highest percent elongation.

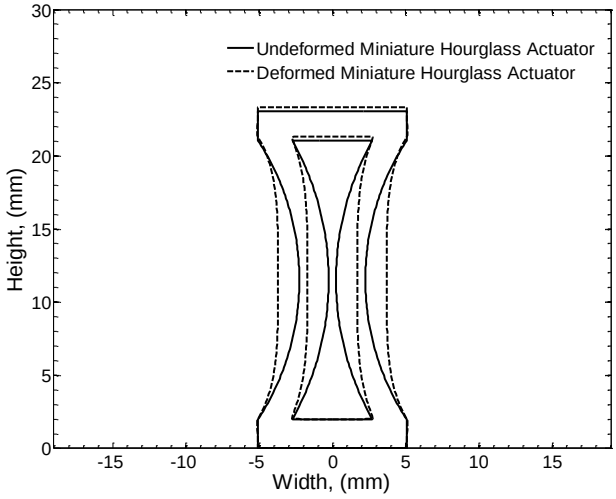

Figure 20. As in Case 1 the geometry of the MHA in Case 2 with the maximum mechanical advantage is the geometry with the straightest side-walls $\alpha=11\pi/32$. The elongation is also small at on 1.22%.

Figure 21 shows that the MHA can elongate up to 0.28 mm with 7 displacement steps. This small elongation is typical of the MHA that produce the highest blocked mechanical advantages. In addition the work density achieved was calculated to be 0.173 MJ/m^3, approximately 5% higher than the Case 1 maximum mechanical advantage geometry. The blocked force of 166 N/mm, however, is lower than Case 1 which has a blocked force of 185 N/mm. The force per unit length drops from 166 N/mm to 118 N/mm which is a decrease of 29%. It does, however, remain much higher than the 27.2 N/mm of the Comparable Traditional Actuator.

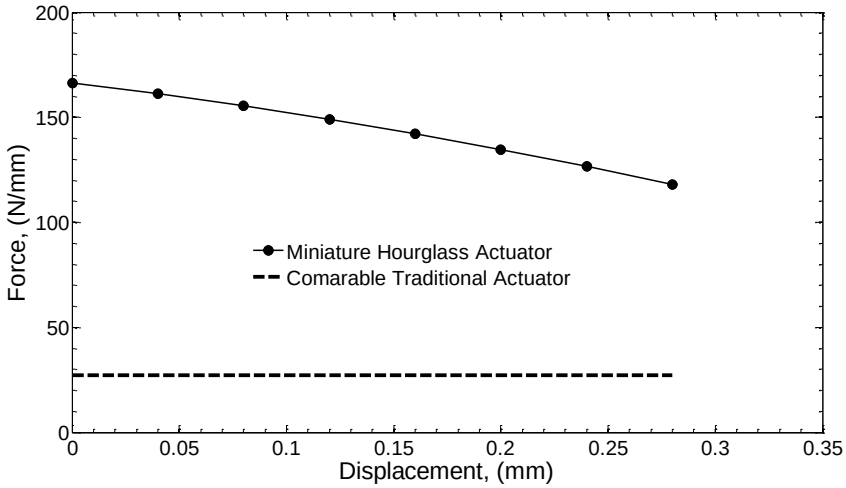

Figure 21. For the Case 2 MHA with maximum mechanical advantage the blocked force is 166 N/mm that drops to 118 N/mm over a distance of 0.28 mm. Even though the force remains high the work density is low because it is limited by the small elongation.

4.2.2 Case 2. Constant MHA Side-Wall Arc Length Maximum Percent Elongation

Figure 22 shows the elongation when the MHA expands the force the MHA can apply goes to zero. The specific MHA geometry studied here does not represent the true maximum elongation to side-wall buckling because at that displacement, the force the MHA could apply would be negative, meaning that the MHA had to be pulled apart to get to this point. It can be seen that even at the largest displacement with applied force, there was still insufficient elongation to cause buckling. The MHA could actually displace much more before the side-walls buckled out, but this would require it to be pulled.

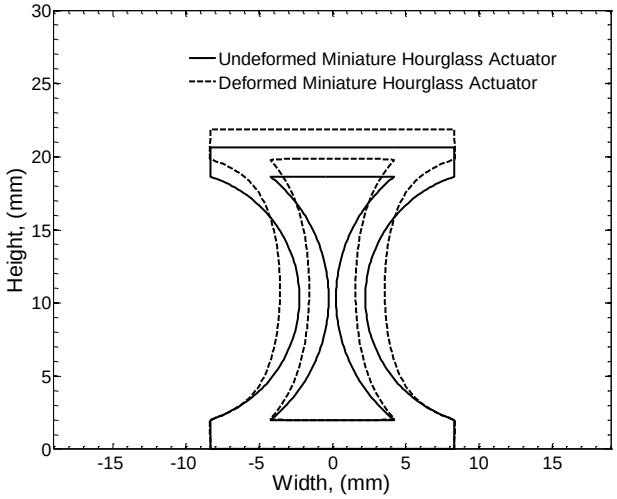

Figure 22. The MHA geometry of Case 2 with the maximum percent elongation has an elongation of 5.62%. The elongation is not limited by the initiation of side-wall buckling but by the force that the MHA could supply dropping to zero.

The MHA geometry that gives the maximum percent elongation in Case 2 has an arc angle of $\alpha=21\pi/32$ similar to that of the highest elongating geometry in Case 1. In Case 2 the arc radius is 9.70 mm compared to 11.66 mm in Case 1. This in turn gave Case 2 a smaller arc length of 20.0 m versus Case 1's 24.0 mm, which explains the lower maximum percent elongation in Case 2 of 5.62% contrasted to the 8.67% in Case 1. The same arc angle but a smaller radius in Case 2 leads to a larger side-wall curvature. This is interesting as the elongation during side-wall buckling is longer than in Case 1. However, at such elongations, the force that the MHA was able to apply went to zero before the side-walls began to buckle out rendering further MHA expansion valueless. Therefore, only the elongation with positive force was considered.

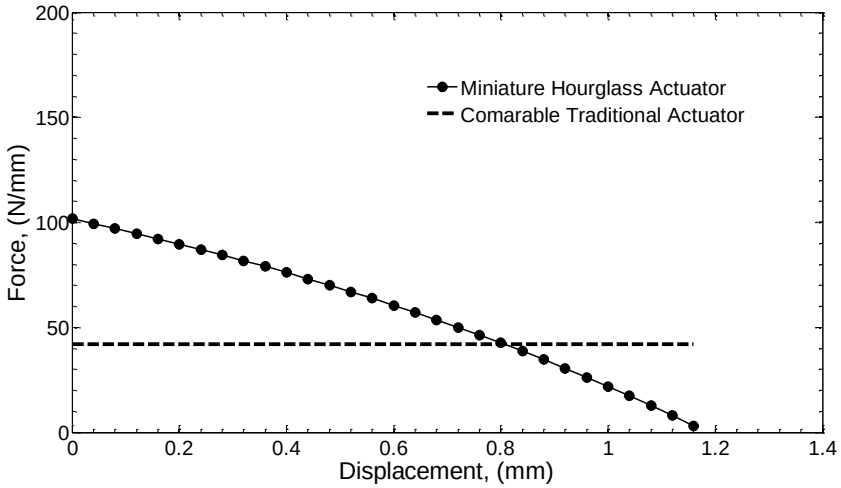

Figure 23. In Case 2 the MHA with maximum percent elongation has a blocked force of 102 N/mm which decreases by 97% to 3.15 N/mm over an elongation of 1.16 mm. This force decrease is also more linear than other cases like because the side-walls never get a chance to straighten out.

4.2.3 Case 2. Constant MHA Side-Wall Arc Length Maximum Work Density

For Case 2 the maximum work density MHA geometry is shown in Figure 24. Similar to the previous geometry in this simulation the force went to zero before side-wall buckling occurred. The work density achieved by this Case 2 MHA geometry is 0.294 MJ/m^3. This work density is 48% higher than the maximum percent elongation work density and the elongation is only slightly less at 4.10% compared to 5.62%. The maximum work density geometry also has a blocked force of 140 N/mm which is only 16% lower than the 166 N/mm exhibited by the maximum mechanical advantage geometry.

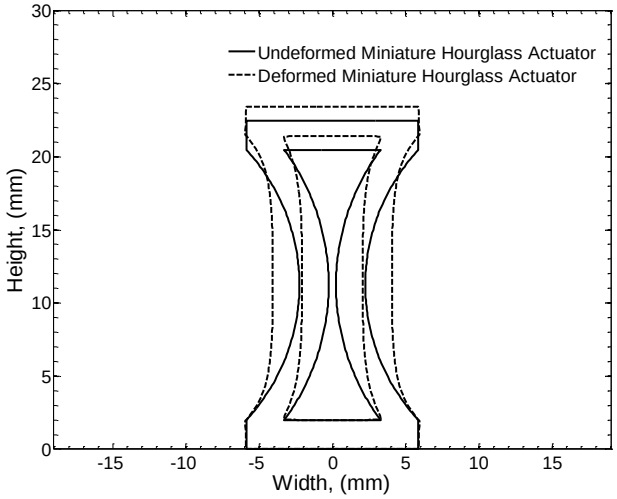

Figure 24. The MHA geometry of Case 2 with the maximum work density is only able to reach an elongation of 0.92 mm or 4.10% before the side-walls begin buckling out. This easier buckling that limits elongation is likely caused by a MHA that is taller than the Case 1 MHA.

Figure 25 below shows a smooth decline to a force that is very close to zero. Note that the decline is not as linear as the maximum mechanical advantage or the maximum percent elongation geometries. This is expected because both of these simulations show that as the force decreases approximately linearly as the side-wall curvature increases. This linear behavior is cause by the side-walls start to buckle outward early, before they get too close to straight, which prevent the force from declining sharply.

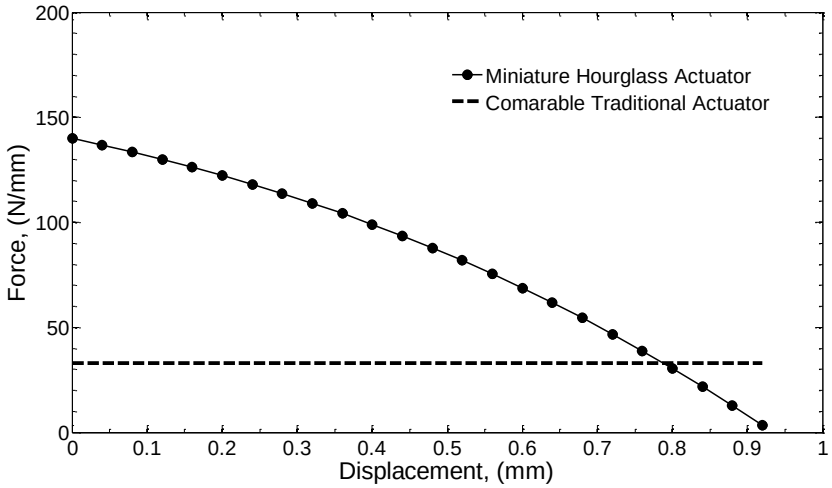

Figure 25. At an elongation of about 7.9 mm the MHA force drops below that of the CTA. This decline in force and an elongation of 4.10% yield a work density of 0.294 MJ/m^3 which is the lowest maximum work density of the 3 cases studied.

4.2.4 Case 2 MHA Mechanical Advantage and Work Density

The percent elongation first increases with an increase in arc angle at a sharp pace but then levels out at larger arc angles. Unlike Case 1 where the percent elongation continues to increase with an increase arc angle the Case 2 percent elongation only increases slowly after an arc angle of $\alpha=14\pi/32$. This is because in Case 1 the arc length continues to increase with an increase in arc angle. This is necessary to keep the MHA height constant. In Case 2, however, the arc length is fixed so the MHA height decreases with increase in arc angle. These factors allow the Case 1 MHAs percent elongation to be a stronger function of arc angle. The force and work advantage from Case 1 and Case 2 follow similar trends and have similar values at the same arc angle. This shows that they are both more of a function of side-wall shape than side-wall arc length or MHA height.

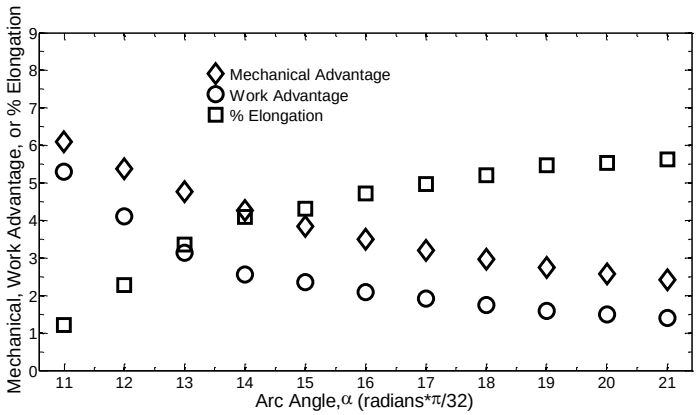

Figure 26. The mechanical advantage, work advantage, and percent elongation for Case 2 plotted against the arc angle show a trend similar to Case 1 where the force and work advantage decline and the percent elongation increase with an increase in arc angle.

In Case 2, when the arc length is held constant instead of the height, the maximum work density occurs at $\alpha=14\pi/32$ compared to $\alpha=18\pi/32$ in Case 1. The work density as a function of arc angle is also very different for these two cases. As seen in Figure 27 the work density declines after the peak that occurs at $\alpha=14\pi/32$ unlike in Case 1 where the curve stays level for the geometries after the peak. In Case 2 the work density achieved by the comparable traditional actuator increases slowly at first but then levels off in contrast with Case 1 where it increases at a consistently nearly linear pace. A summary of Case 2 results is presented in Table 5.

As discussed for Case 1 in Case 2 the work density of the Comparable Traditional Actuator in Case 2 follows the same trend as the percent elongation. Again this is because the work density is a function of the force and displacement and the force is fixed for the CTA. The reason the force is fixed is because it is set equal to the pressure acting on the top inner surface of the MHA.

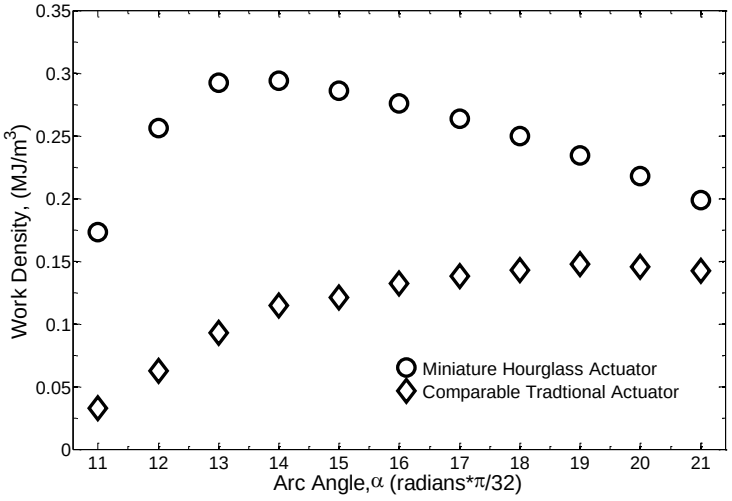

Figure 27. The MHA and comparable traditional actuator work density for Case 2 Plotted Against Arc Angle. The highest work density occurs at an arc angle of $\alpha=14\pi/32$ in Case 2 compared to $\alpha=18\pi/32$ for Case 1. The MHA work is higher than the CTA work for all arc angles.

In Case 2 not only does the work density follow a much different trend but it never reaches values as large as that in Case 1. In Case 2 the maximum work density of 0.294 MJ/m^3 occurs at $\alpha=14\pi/32$ which is the arc angle where the percent elongation begins to increase at a slower rate. In Case 1, where the percent elongation continues to increase at an almost constant rate, the maximum work density of 0.396 MJ/m^3 occurs at a larger arc angle of $\alpha=18\pi/32$.

Table 5. Results for Case 2 analysis covered arc angles from 11π/32 to 21π/32 and had a constant MHA side-wall arc length of 20.0 mm.

Arc Angle α	Blocked Force (N/mm)	Mechanical Advantage	Work Advantage	Elongation (mm)	% Elongation	Work Density (MJ/m^3)	Comparable Traditional Actuator Work Density (MJ/m^3)
11π/32	166	6.10	5.29	0.28	1.22	0.173	0.033
12π/32	157	5.37	4.11	0.52	2.27	0.256	0.062
13π/32	148	4.76	3.14	0.76	3.35	0.292	0.093
14π/32	140	4.26	2.57	0.92	4.10	0.294	0.114
15π/32	133	3.85	2.36	0.96	4.32	0.286	0.121
16π/32	126	3.50	2.09	1.04	4.73	0.276	0.132
17π/32	120	3.21	1.91	1.08	4.96	0.263	0.138
18π/32	115	2.96	1.75	1.12	5.21	0.250	0.143
19π/32	110	2.75	1.59	1.16	5.47	0.234	0.147
20π/32	106	2.57	1.50	1.16	5.54	0.218	0.146
21π/32	102	2.42	1.40	1.16	5.62	0.199	0.142

4.3 Case 3. MHA Side-Wall Thickness Variation

For Case 3 the geometry of $\alpha=18\pi/32$ and r=12.94 mm was chosen from Case1 because it was the geometry that achieved the highest work density. In Case 1 the side-wall thickness t was equal to 2 mm so for Case 3 the side-wall thickness was varied between 1.6 mm and 2.4 mm in 0.1 mm steps.

4.3.1 Case 3. MHA Side-Wall Thickness Variation Maximum Mechanical Advantage

The maximum mechanical advantage in Case 3 of 3.11 occurs at a wall thickness of 1.6 mm. It is less than 6% greater than the lowest Case 3 mechanical advantage of 2.94 at a wall thickness of 2.4 mm. Figure 28 shows the geometry of Case 3 maximum mechanical advantage. This MHA exhibits a blocked force per unit length of 142 N/mm which is 3.11 times larger than the force per unit length from the pressure acting on the MHAs top inner surface. It is able to accomplish 3.25 times more than the Comparable Traditional Actuator with a work density of 0.330 MJ/m^3 and a percent elongation of 3.17%.

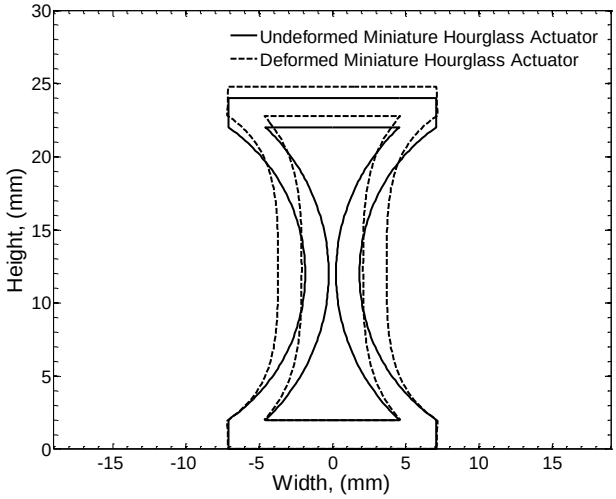

Figure 28. This geometry with a side-wall thickness of 1.6 mm is the Case 3 MHA with the maximum mechanical advantage has the thinnest side-wall of any geometry studied. This allows it to expand more easily but the side-walls begin to buckle out easily as well.

This geometry with t=1.6 mm is a very interesting one because the force actually goes up until the elongation stops. The thinner side-wall still adds the mechanical advantage and lets the MHA expand more easily. As the side-walls straighten they are able to transfer more force to the MHA ends making supplied force increase. This behavior is illustrated in Figure 29. The t=1.6 mm geometry is the only geometry discussed where this force increase occurs.

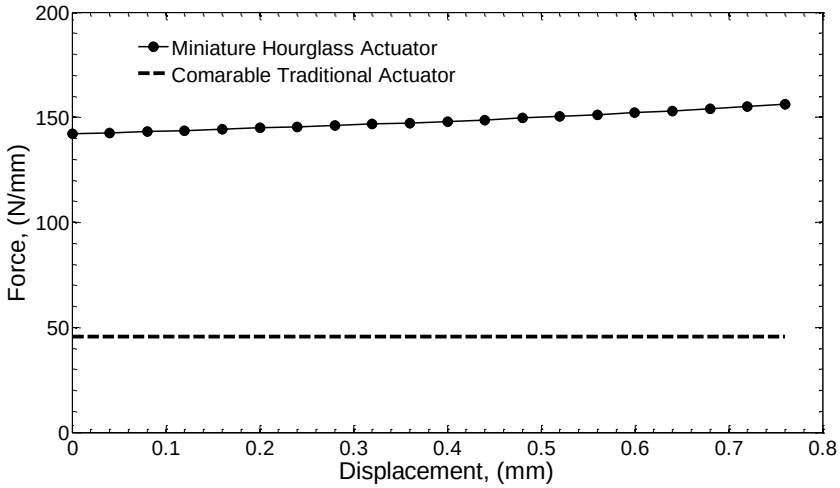

Figure 29. In this unique result the force increases with elongation by 10% and is the only geometry where this occurs. The side-wall thickness is 1.6 mm which is 20% thinner than the side-wall thicknesses in Case 1 and 2. This allows the MHA to expand more easily but the side-walls begin to buckle out at an elongation of only 3.17%.

4.3.2 Case 3. MHA Side-Wall Thickness Variation Maximum Percent Elongation

Shown in Figure 30, the Case 3 geometry that elongates the most is the t=2.0 mm MHA. This is the same geometry of the maximum work density MHA of Case 2. The percent elongation is 6.67%. The mechanical advantage and work density are 3.02 and 0.396 MJ/m^3 respectively. The wall thickness effect on percent elongation is a result of when side-wall buckling occurs for thinner side-walls and a function of the side-wall bending stiffness for thicker side-walls.

The force and displacement curve for the Case 3 maximum percent elongation is shown in Figure 31. This curve shows a decline in force that is slow at first but then becomes sharper as the MHA elongates which is typical for all maximum elongation geometries considered. The force drops below the force a comparable traditional actuator could supply at an elongation of 1.38 mm. As seen for some of the previously

discussed geometries there is a sharper change in slope between the elongations of 1.44 mm and 1.48 mm followed by a return to the previous curve trend. Again, the reason for this is unknown.

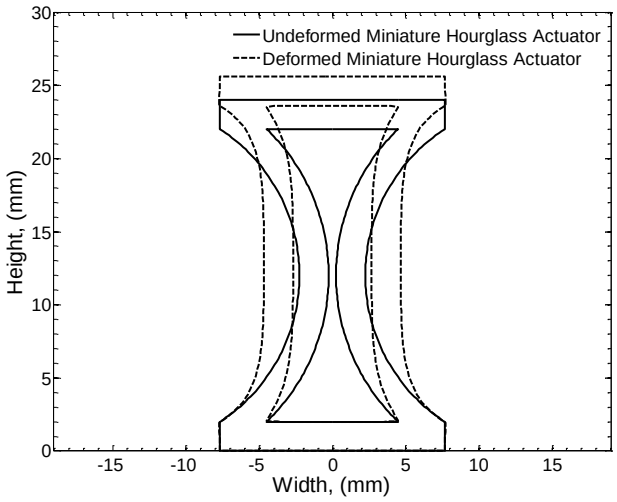

Figure 30. When the side-wall thickness is 2.0 mm the MHA can expand by 1.6 mm or 6.67% before the side-walls begin to buckle out. However, this does not create the highest work density for Case 3 because the force drops sharply.

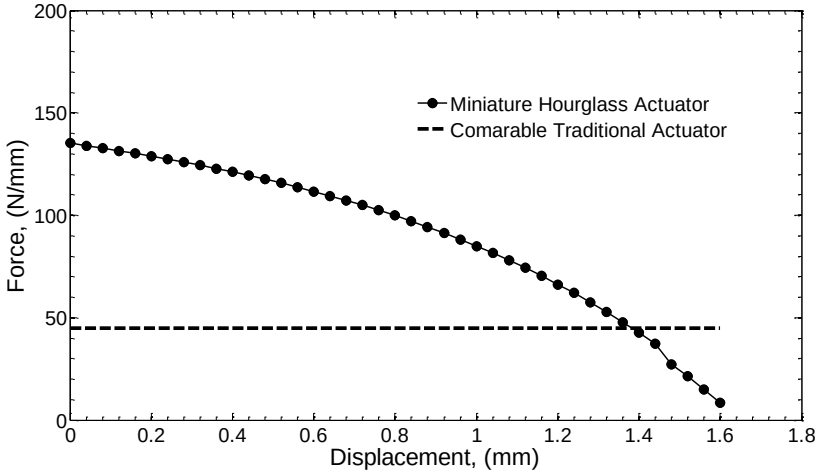

Figure 31. The force in the maximum percent elongation geometry in Case 3 drops from 135.2 to 8.4 N/mm which is a drop of 94% even with a elongation of only 6.67%. Even though the elongation is only slightly more than the highest work density MHA the force drop is much larger.

4.3.3 Case 3. MHA Side-Wall Thickness Variation Maximum Work Density

Case 3 had the MHA geometry with the highest work density at 0.434 MJ/m^3. This occurred at a side-wall thickness of t=1.9 mm. However, a side-wall thickness of t=1.8 mm the work density is nearly as high at 0.433 MJ/m^3. Suggesting that there might be some thickness between the two which demonstrates a slightly higher work density, this however was not investigated. Figure 32 shows this MHA geometry with the highest work density. This MHA geometry had an elongation of 5.83% and a blocked mechanical advantage of 3.04. It actually was able to elongate slightly less than the 6.67% form Case 2 with the same arc angle and radius. Its wall thickness was slightly less which made the mechanical advantage higher than the 3.02 but also allowed the walls to buckle at a lower elongation. The combination of these factors still gave the t=1.9 mm MHA about a 10% higher work density.

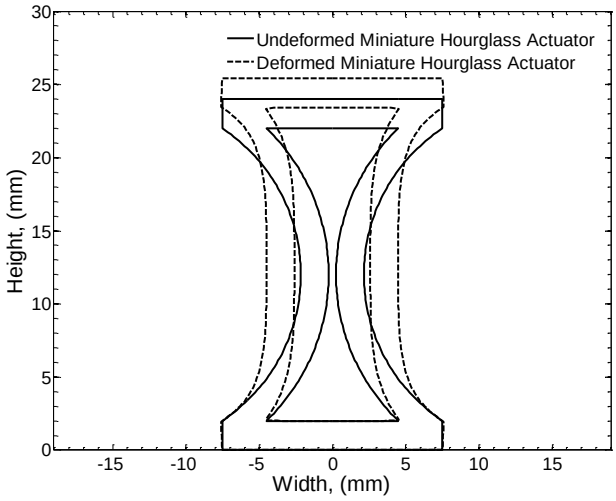

Figure 32. The free expansion of this MHA is stopped before the force reaches zero because the side-walls begin to buckle outward. When the MHA expansion is stopped the elongation is 1.4 mm or 5.83% and the force applied by the MHA is 65.7 N/mm.

The geometry in Case 3 that yields the maximum work density has a wall thickness, arc angle, arc radius of t=1.9 mm, $\alpha=18\pi/32$, and r=12.94 respectively. The work density is 0.434 MJ/m^3 which is only slightly higher the 0.433 MJ/m^3 predicted for the t=1.8 mm side-wall thickness. A characteristic that stand out is only one of the three maximum work density geometries whose force never drops below the force applied to the MHA's moving surface. This can be seen Figure 33 below. Notice that the MHA data set never reaches the force shown for the comparable traditional actuator. Also the force does not drop off as quickly as other geometries when the MHA expands. It drops by more than 50% but this is less than many geometries. The MHA is still able to apply a force of over 60 N/mm when is reach its full expansion just before side-walls begin to buckle out.

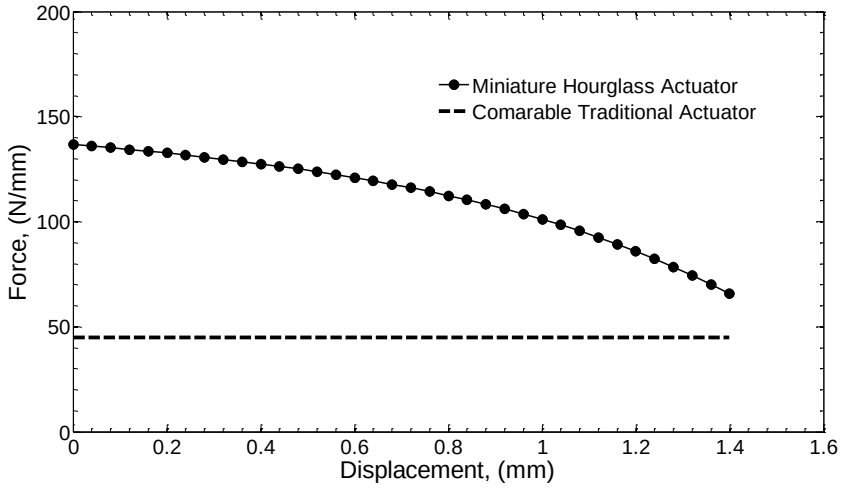

Figure 33. For the maximum work density geometry, t=1.9 mm, in Case 3 the MHA force declines by 52% but stays above the force for a CTA. This MHA elongates by 1.4 mm which is 5.83% of its original height. The combination of elongation and force yield a high work density.

4.3.4 Case 3 MHA Mechanical Advantage and Work Density

The results for the three geometries of maximum mechanical advantage, maximum percent elongation, and maximum work density have all been analyzed and presented here for all three cases. While this is not an exhaustive study on the effects the MHA geometry. It does, however, set forth a substantial foundation to start to understand what parameters can be optimized to affect various MHA responses.

Illustrated in Figure 34 the mechanical advantage is almost independent of side-wall thickness. This might be only true in the range of wall thicknesses studied. If the MHA side-wall is too thin it would not be stiff enough to help apply force as the MHA deformed and if it is too thick the internal pressure would not be able to deform the side-wall therefore not transferring the load to the MHA ends. Second, the work advantage is also not a strong function of side-wall thickness. It decreases slightly as the thickness increases but levels out as the thickness further increases. On the other hand, the percent elongation is a strong function of the side-wall thickness. It is clearly seen in Figure 34 that a wall thickness of 2.0 mm has the highest percent elongation of 6.67% which decreases to 3.17% for the 1.6 mm wall thickness and 4.67% for the 2.4 mm wall thickness. When the wall is thin, it bows out easily, limiting the elongation. Alternately if it is thick it is difficult to bend limiting elongation.

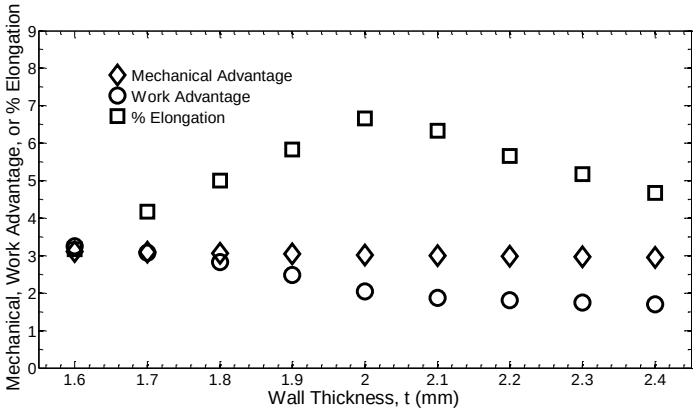

Figure 34. Although both decrease slightly with increase in side-wall thickness neither the force or work advantage is that dependant on side-wall thickness. Reaching a peak a t=2.0 mm the percent elongation is a strong function of side-wall thickness.

The work density of MHA studied in Case 3, which is plotted in Figure 35, shows a large variation with side-wall thickness. The largest work density of 0.434 MJ/m^3 appears at a wall thickness of 1.9 mm which is negligibly higher than the work density of 0.433 MJ/m^3 that a wall thickness of 1.8 mm can achieve. This is evidence that the actual maximum occurs somewhere between the two points but no more simulations were done to investigate it. The work density drops significantly in both directions. It falls to 0.211 MJ/m^3 at t=2.4 mm and 0.330 MJ/m^3 at t=1.6 mm. Again, the work density of the Comparable Traditional Actuator follows the percent elongation. Table 6 summarizes the results of Case 3.

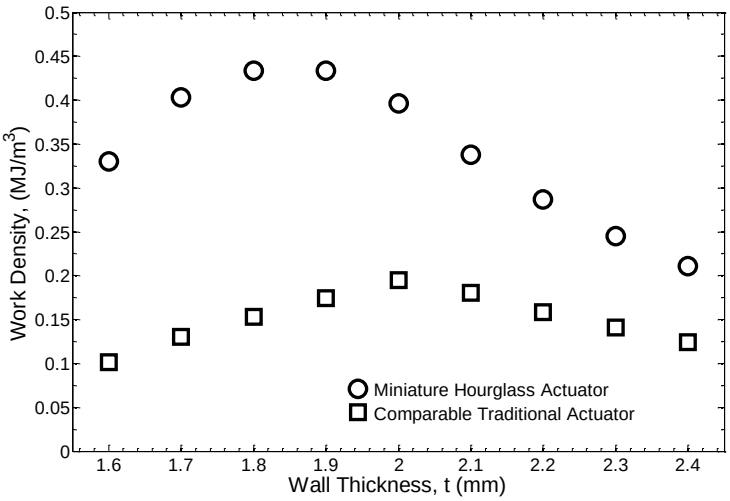

Figure 35. The work density for Case 3 is a clear function of the side-wall thickness reaching a maximum at t=1.9 mm. Since the mechanical advantage is not that dependant on side-wall thickness the main contributor to this result is the percent elongation being a strong function of side-wall thickness.

An interesting thing to note is that from a change in side-wall thickness from t=1.9 mm to t=2.0 mm the work density decreases by 8.8% from 0.434 MJ/m^3 to 0.396 MJ/m^3 even though the blocked forces are nearly equal at 137 N/mm compared to 135 N/mm and the percent elongation increased from 5.83% to 6.67%. The reason for this drop in work density must then be a result of a quicker drop in force as the MHA elongates for the t=2.0 mm geometry.

Table 6. Results for Case 3 analysis which cover side-wall thicknesses from 1.6 to 2.4 mm with $\alpha=18\pi/32$ and r=12.94 mm.

Side-Wall Thickness (mm)	Blocked Force (N/mm)	Mechanical Advantage	Work Advantage	Elongation (mm)	% Elongation	Work Density (MJ/m^3)	Comparable Traditional Actuator Work Density (MJ/m^3)
1.6	142	3.11	3.25	0.76	3.17	0.330	0.102
1.7	140	3.09	3.08	1.00	4.17	0.403	0.131
1.8	138	3.06	2.83	1.20	5.00	0.433	0.153
1.9	137	3.04	2.49	1.40	5.83	0.434	0.174
2	135	3.02	2.03	1.60	6.67	0.396	0.195
2.1	134	3.00	1.87	1.52	6.33	0.337	0.181
2.2	132	2.98	1.81	1.36	5.67	0.287	0.158
2.3	131	2.96	1.74	1.24	5.17	0.245	0.141
2.4	129	2.94	1.70	1.12	4.67	0.211	0.124

5. CONCLUSION AND FUTURE WORK

5.1 Conclusion

The highest mechanical advantage occurs for the geometry with the smallest arc angle in both Case 1 and Case 2. These geometries correspond to the MHAs with the straightest side-walls. The largest work advantage occurs for the same MHA geometries as the highest mechanical advantage. In Case 3 the mechanical advantage remains almost the same for all MHA side-wall thicknesses and the work advantage only decreases slightly with increase in wall thickness. In some configurations and cases they are stronger functions than in others. In both Case 1 and Case 2 the mechanical advantage declined with increasing arc angle. This means that the straighter side-walls transferred more of the force from pressure on them onto the ends of the MHA. This is obviously only true to a point. If the side-walls were completely straight they would not be able to push the MHA ends at all because they would bow out not straighten. The investigation done in this study did not simulate any MHAs with side-walls straight enough to see the decline mechanical advantage. In Case 3 the mechanical advantage is almost unchanged by changing the side-wall thickness. This supports the evidence given by the first two cases that the side-wall shape dominates MHAs ability to supply a force larger than the pressure acting on the inner end surface.

The work advantage also followed the same trend as mechanical advantage in Case 1 and Case 2. This is for a different reason though. Since the elongation goes up as the arc angle increases the force becomes less dominate in the work MHA can perform. Also the work that the comparable actuator can achieve increases with the rise in

elongation. These two factors make the ratio of MHA work to the work of the comparable traditional actuator drop. In Case 3 the work advantage drops as with the drop in elongation. This is because drop in elongation affects the MHA work more than the work of the comparable traditional actuator.

In Case 1 and Case 2 the geometries that achieve the maximum elongation are the two geometries that have the largest arc angle the smallest arc radius in each case. This allows the MHA to expand more before the side-walls buckle out. For these cases the force also gets close to zero before the elongation stops. This is important to note because the MHA might not be useable through the entire elongation if the force drops below the necessary force required. In Case 3 the MHA with the highest elongation occurs at a wall thickness of 2 mm. This is because thinner walls buckle out more easily and the thicker side-walls are more difficult to straighten during elongation.

For all MHA geometries the work density is higher than the comparable traditional actuator work density. The geometries in Case 1 and Case 2 with the highest work density have arc angles between the arc angles that have the largest mechanical advantage and percent elongation. For every MHA the force it can supply decreases as it elongates. The MHAs with the highest work densities are all geometries that are able to display moderate force coupled with moderate elongation.

From the study performed it is evident that all the performance characteristics of the MHA are a function of MHA geometry. In order for the MHA to be implemented in a successful and optimized design more work needs to be done to study the MHA behavior. Also, well defined design necessity would need to be developed so that a clear

picture of what needs to be optimized is available. The miniature hourglass shaped actuator has potential if its design can be refined and optimized for a specific low elongation high force application.

5.2 Future Work

The end goal is the design of arrays of MHAs that could be embedded in a matrix material to create multifunctional materials that can perform the task of being both the actuator and the structure. Design scheme needs to be done. Deformation analysis would be useful to figure out MHA placement inside the material. There must be a way to design, optimize and simulate the behavior of an MHA array.

Experiments also need to be done to validate the predictions of the finite element code. Experiments would also allow more insight into issues that are not addressed with modeling such as: How to cap the ends to contain the internal pressure and see how this affects the MHA behavior, Can the MHA be manufactured reasonably easy, how much actuation time is required.

Materials also need to be studied and optimized to get desirable MHA behavior. There is a possibility that some orthotropic material might allow the MHA to achieve better performance like longer elongation before side-wall bucking. The study done does not address any material issues, which forms a critical aspect of the functionality. In order to create a useful MHA many questions would need to be addressed. For example, is there a real material that can undergo the deformations and what material properties would make the MHA work best? A material study could be very extensive.

Modeling an axisymmetric instead of a plane strain MHA would be a valuable. This would change the geometry of the MHA from long to round. An axisymmetric MHA might allow the MHA to be incorporated in a wider range of designs. If it was modeled as axisymmetric end effects would be considered. An axisymmetric MHA could increase the number of possible applications where MHAs could be used, MHA modeled in this study. The axisymetric MHA geometry is shown in Figure 36.

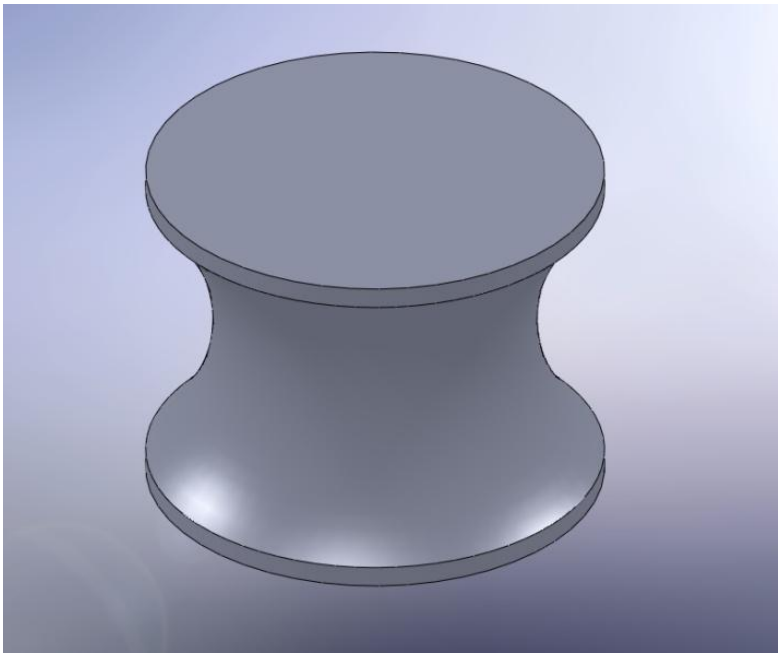

Figure 36. The axisymmetric MHA is a smaller unit that could be incorporated in a more complex array of actuators. An axisymmetric MHA also would not have any end effects because there is no need for a sealed end termination.

This study of how geometries changes affect the behavior of the miniature hourglass actuator provides a basis for comprehension of how to design the MHA with avenues for future works to explore.

REFERENCES

[1] D. M. McCutcheon, Machine Augemented Composites for Damping Purposes, MS Thesis, Texas A&M University, College Station **2004**.

[2] J. E. Huber, N. A. Fleck, M. F. Ashby, *Proc. R. Soc. London Ser. A-Mat. Phy. Eng. Sci.* **1997**, *453*, 2185-2205.

[3] B. L. Lee, D. J. Inman, *Proc. Inst. Mech. Eng. Part I-J Syst Control Eng*. **2009**, *223*, 431-434.

[4] L. Christodoulou, J. D. Venables, *JOM.* **2003**, *55*, 39-45.

[5] B. S. Hill, G. P. Findlay, *Q. Rev. Biophys*. **1981**, *14*, 173-222.

[6] I. Burgert, P. Fratzl, Philos. Trans. R. *Soc. A-Math. Phys. Eng. Sci.* **2009**, *367*, 1541-1557.

[7] Y. Forterre, J. M. Skotheim, J. Dumais, L. Mahadevan, *Nature* **2005**, *433*, 421-425.

[8] W. R. Fagerberg, D. Allain, *Am. J. Bot*. **1991**, *78*, 647-657.

[9] R. D. Allen, *Plant Physiol*. **1969**, *44*, 1101-1107.

[10] H. S. Patil, S. Vaijapurkar, *J. Bionic Eng*. **2007**, *4*, 19-23.

[11] Y. Bar-Cohen, *Bioinspir. Biomim.* **2006**, *1*, 1-12.

[12] S. Nemat-Nasser, S. Nemat-Nasser, T. Plaisted, A. Starr, A. V. Amirkhizi, *Biomimetics - Biologically Inspired Technologies*, (Ed: E. Y. Bar-Cohen), CRC Press, Boca Raton, FL **2005**, 309-338.

[13] M. A. Meyers, A. Y. M. Lin, Y. Seki, P. Y. Chen, B. K. Kad, S. Bodde, *JOM.* **2006**, *58*, 35-41.

[14] A. V. Srinivasan, G. K. Haritos, F. L. Hedberg, *Appl. Mech. Rev.* **1991**, *44*, 463-482.

[15] Y. R. Lin, H. A. Sodano, Compos. *Sci. Technol*. **2009**, *69*, 1825-1830.

[16] P. T. Curtis, Adv. *Perform. Mater*. **1996**, *3*, 279-293.

[17] C. C. Seepersad, B. M. Dempsey, J. K. Allen, F. Mistree, D. L. McDowell, *AIAA J.* **2004**, *42*, 1025-1033.

[18] R. S. Kumar, D. L. McDowell, *Int. J. Solids Struct.* **2009**, *46*, 2871-2885.

[19] V. Giurgiutiu, L. Mathews, D. J. Leo, V. B. Sundaresan, Concepts for Power and Energy Analysis in Nastic Structures, presented at *ASME International Mechanical Engineering Congress and Exposition*, Orlando, FL, November 5-11, **2005**, *70*, 421-428.

[20] M. W. Hyer, A. Jilani, *Smart Mater. Struct* **1998**, *7*, 784-791.

[21] M. R. Hassan, F. Scarpa, M. Ruzzene, N. A. Mohammed, *Mater. Sci. Eng., A*, **2008**, *481-482*,654-657.

[22] S. Hirai, T. Masui, S. Kawamura, Prototyping Pneumatic Group Actuators Composed of Multiple Single-motion Elastic Tubes, presented at *International Conference on Robotics and Automation*, Seoul, Korea, May21-26, **2001**, *4*, 3807-3812.

[23] D. M. McCutcheon, J. N. Reddy, M. J. O'Brien, T. S. Creasy, G. F. Hawkins, J. *Sound Vibr*. **2006**, *294*, 828-840.

[24] J. H. Kim, Passive Machine Augemented Composistes for Muultifunctional Properties, PhD Dissertation, Texas A&M University, College Station **2005**.

[25] C. Y. Tang, M. J. O'Brien, G. F. Hawkins, *JOM.* **2005**, *57*, 32-35.

[26] C. Thill, J. Etches, I. Bond, K. Potter, P. Weaver, *Aeronaut. J.* **2008**, *112*, 117-139.

[27] D. Baker, M. I. Friswell, *Smart Mater. Struct.* **2009**, *18*, 1-13.

[28] D. Inoyama, B. P. Sanders, J. J. Joo, *J. Aircraft.* **2007**, *44*, 1205-1213.

[29] D. Cadogan, T. Smith, F. Uhelsky, M. Mackusick, Morphing Inflatable Wing Development for Compact Package Unmanned Aerial Vehicles, presented at *45th AIAA/ASME/ASCE/AHS/ACS Structures, Structural Dynamics & Materials Conference*, Palm Springs, CA, April 19-22, **2004**, *1*,1-13

[30] T. Yokozeki, S. Takeda, T. Ogasawara, T. Ishikawa, *Compos. Pt. A-Appl. Sci. Manuf.* **2006**, *37*, 1578-1586.

[31] A. C. H. Leung, S. D. Guest, *J. Mech. Mater. Struct*. **2007**, *2*, 303-317.

[32] J. N. Reddy, *An Introduction to the Finite Element Method*, McGraw-Hill Higher Education, New York, NY **2006**.

[33] J. N. Reddy, *An Introduction to Nonlinear Finite Element Analysis*, Oxford University Press, New York, NY **2004**.

[34] R. D. Cook, *Concepts and Applications of Finite Element Analysis*, Wiley, New York, NY **2001**.

[35] A. Palazzolo,"MEMA 647 Class Notes", Texas A&M University, College Station **2007**.

[36] G. Payette, On the Integration of Traction Vectors Along the Boundaries of Two-Dimensional High Order Finite Elements, Unpublished Notes, Texas A&M University,College Station **2009**.

[37] K. Schweizerhof, E. Ramm, *Comput. Struc.t* **1984**, 18, 1099-1114.

[38] J. C. Simo, R. L. Taylor, P. *Wriggers, Commun. Appl. Numer. Methods.* **1991**, *7*, 513-525.

[39] J. E. Shigley, C. R. Mischke, R. G. Budynas, *Mechanical Engineering Design*, McGraw-Hill, New York, NY **2004**.

APPENDIX A

2D MINIATURE HOURGLASS ACTUATOR SIMULATION MAIN PROGRAM

```
%                                                    Roston Elwell
2/27/09

%2D Miniature Hourglass Actuator Simulation
clc
clear all
close all

tic;

%User Input
Problem='Mechanical Advantage, Elongation, and Work of a
pressurized MHA';
Discription='MHA with uniform internal pressure modeled in plane
strain';

%Material Properties
Ey=2000;    %Young's Modulus
v=0.3;      %Possion's Ratio
SS=2;       %SS-State of Stress 1-Plane Stress  2-Plane Strain 3-
Axisymmetric
Material=[Ey v SS];

%Geometry
r=14.44;                        %radius of side wall arc
t=2.0;                          %thickness of side wall
alpha=16*pi/32;                 %arc angle
R=(r*(1-cos(alpha/2))+t/2+.25); %1/2 HCE width or diameter
T=2;                            %thickness of bottom
d=1;                            %plane stress/strain thickness
Geometry=[r t alpha R T d];

%Load
p=5;            %uniform internal pressure
UIG=0;          %U Intial Guess/starting point for all non-
specified primary variables
DSS=.02;        %Displacement Step Size

%Element Type Information
%this program is only set up for ET=2, NDOFPN=2, and NNPE=9 do not
change these inputs
ET=2;           %Element Type:1 for linear 2 for quadratic
NDOFPN=2;       %Number of Degrees Of Freedom Per Node
NNPE=9;         %Number of Nodes Per Element
```

```
NGP=3;          %Number of Gauss Points in each direction to be
used in full intergration
ETI=[ET NDOFPN NNPE NGP];

%Element Mesh Information
EMI(1)=24;      %Number of Elements Along Arc
EMI(2)=4;       %Number of Elements Through Arc
EMI(3)=9;       %Number of Elements Along Bottom
EMI(4)=3;       %Number of Elements Through Bottom

%Finite Element Method Information
Epsilon=10E-4;  %Epsilon is the convergence tolerance
MNI=10;         %MNI-maximum nuber of iterations for solution to
converge
NLS(1)=5;       %NLS(1)-Number of Load Steps for Situation 1
NLS(2)=100;     %NLS(2)-Maximum Number of Load Steps for Situation
2

%End of User Input

%create an array of element sides where internal pressure is
applied
[PSide]=PressureSide(EMI);

%generate the mesh and corresponding arrays
[NC,NCA,DOFCA,NE,TNN,NOAS,NOAR,NOHIS,NOHB]=MHA_MESH_GENERATOR(Geome
try,EMI);

%create symmetry boundary condition arrays
[DOFSPV,VSPV]=BoundaryCondition(NOAS,NOAR,NOHB);

%create stepped displacement boundary condition arrays
[DOFSBD,VSBD]=SteppedBottomDisplacementBC(NOHB);

%This program is not set up to handle specified point loads

%assign intial values
U(1:TNN*NDOFPN,1)=UIG;
NC_1=NC;

%Situation Loop
for Situation=1:2
    %preallocate array for storing data for each situation and load
step
    if Situation==1
        ConvergenceInformation1=ones(1,NLS(1));
        NC_Results1=zeros(TNN,2,NLS(1));
    end

    if Situation==2
        ConvergenceInformation2=ones(1,NLS(2));
```

```
        NC_Results2=zeros(TNN,2,NLS(2));
        UYLS=zeros(NLS(2),1);
        FYLS=zeros(NLS(2),1);
    end

%Load Step Loop
LS=0;
LoadStepLoopGo=1;
while LS<NLS(Situation) && LoadStepLoopGo==1
    LS=LS+1;

    if Situation==1 %blocked displacement
        P=LS*p/NLS(1);
        ADOFSPV=horzcat(DOFSPV,DOFSBD);
        VSBD(1:length(NOHB))=0;
        AVSPV=horzcat(VSPV,VSBD);
    end

    if Situation==2 %stepped expansion
        P=p;
        ADOFSPV=horzcat(DOFSPV,DOFSBD);
        VSBD(1:length(NOHB))=-DSS*LS;
        AVSPV=horzcat(VSPV,VSBD);
    end

%Iteration Loop
Iteration=0;
IterationLoopGo=1;
while Iteration<MNI && IterationLoopGo==1
    Iteration=Iteration+1;
    disp('Situation, Load Step, Iteration')
    disp(Situation)
    disp(LS)
    disp(Iteration)

%preallocating arrays for the coordinates and values of the global
%stiffness matrix and force vecter
IK=zeros(NE*(NNPE*NDOFPN)^2,1);
JK=zeros(NE*(NNPE*NDOFPN)^2,1);
VK=zeros(NE*(NNPE*NDOFPN)^2,1);
Kcoordinate_count=0;
IF=zeros(NE*NNPE*NDOFPN,1);
VF=zeros(NE*NNPE*NDOFPN,1);
Fcoordinate_count=0;

%perform numerical integration on each of the elements
for E=1:NE

%Element Stiffness
[KE]=ElementStiffnes4UpdatedLagrangian(E,NCA,DOFCA,NC_1,U,ETI,Mater
ial,d);
```

```
%Element Force
[FE]=ElementForce4UpdatedLagrangian(E,NCA,DOFCA,NC_1,U,P,d,ETI,Mate
rial,PSide);

%assemble global stiffness matrix as coordinates and values for
creating a sparse matrix
    for m=1:NNPE*NDOFPN
        i=DOFCA(E,m);
        for n=1:NNPE*NDOFPN
            j=DOFCA(E,n);
            Kcoordinate_count=Kcoordinate_count+1;
            IK(Kcoordinate_count,1)=i;
            JK(Kcoordinate_count,1)=j;
            VK(Kcoordinate_count,1)=KE(m,n);
        end
    end

%assemble the global force vector as coordinates and values for
creating a sparse matrix
    for m=1:NNPE*NDOFPN
        i=DOFCA(E,m);
        Fcoordinate_count=Fcoordinate_count+1;
        IF(Fcoordinate_count,1)=i;
        VF(Fcoordinate_count,1)=FE(m,1);
    end %end m loop

end %end E loop

%create full global stiffness matrix for use in the post
computation of nodal forces
KG=sparse(IK,JK,VK);

%create the codensed form of the global equations and solve
%set the values of K and F in the rows and columns of the specified
degrees
%of freedom to zero so that they can be removed later
for i=1:length(ADOFSPV)
    for j=1:length(VK)
        if IK(j,1)==ADOFSPV(i) || JK(j,1)==ADOFSPV(i)
            VK(j,1)=0;
        end
    end
    for j=1:length(VF)
        if IF(j,1)==ADOFSPV(i)
            VF(j,1)=0;
        end
    end
end
```

```
%create a column vector for reordering the degrees of freedoms
after the
%the specified degrees of freedoms are removed.
Rcount=0;
Rorder=zeros(TNN*NDOFPN,1);
for i=1:TNN*NDOFPN
    if i~=ADOFSPV(1:length(ADOFSPV))
        Rcount=Rcount+1;
        Rorder(i,1)=Rcount;
    end
end

%create the global stiffness matrix and force vector with the rows
and
%columns of the specified degrees of freedom set to zero.
KCZ=sparse(IK,JK,VK,TNN*NDOFPN,TNN*NDOFPN);
FCZ=sparse(IF,1,VF,TNN*NDOFPN,1);

%find all the nonzero entries in of KCZ and FCZ
[IKC,JKC,VKC]=find(KCZ);
[IFC,JFC,VFC]=find(FCZ);

%reorder the sparse matrix coordinates so that there is not gaps
where the
%specified degrees of freedom were removed
RIKC=zeros(length(VKC),1);
RJKC=zeros(length(VKC),1);
for i=1:length(VKC)
    RIKC(i,1)=Rorder(IKC(i,1),1);
    RJKC(i,1)=Rorder(JKC(i,1),1);
end
RIFC=zeros(length(VFC),1);
for i=1:length(VFC)
    RIFC(i,1)=Rorder(IFC(i,1),1);
end

%create the condensed from of the global stiffness matrix and force
vector
%as sparse matrices
KC=sparse(RIKC,RJKC,VKC,TNN*NDOFPN-length(ADOFSPV),TNN*NDOFPN-
length(ADOFSPV));
FC=sparse(RIFC,1,VFC,TNN*NDOFPN-length(ADOFSPV),1);

%solve for the incremental change in U
deltaU=KC\FC;

%reassemble U
%substitute specified primary variables into U
for i=1:length(ADOFSPV)
    U(ADOFSPV(i),1)=AVSPV(1,i);
end %end i loop
```

```
count=0;
for i=1:TNN*NDOFPN
    if i~=ADOFSPV(1,1:length(ADOFSPV))
        count=count+1;
        U(i,1)=U(i,1)+deltaU(count,1);
    end %end if
end %end i loop

%check if the Euclidean Norm is less than the convergence
tolerance, Epsilon
if Iteration~=1
EnormN=0;
EnormD=0;
        for i=1:TNN*NDOFPN
            EnormN=EnormN+(U(i,1)-U_1(i,1))^2;
            EnormD=EnormD+(U(i,1))^2;
        end %end i loop
    Enorm=abs(sqrt(EnormN/EnormD));

                if Enorm<Epsilon
                    IterationLoopGo=0;
                    if Situation==1
                    ConvergenceInformation1(1,LS)=Iteration;
                    end
                    if Situation==2
                    ConvergenceInformation2(1,LS)=Iteration;
                    end
                else
                    if Situation==1
                    ConvergenceInformation1(1,LS)=0;
                    end
                    if Situation==2
                    ConvergenceInformation2(1,LS)=0;
                    end
                    if Iteration==MNI
                        LoadStepLoopGo=0;
                    end
                end
end
%save the U from the previous interation
U_1=U;

%create an array of and save the nodal coordinates of the previous
%interation
for n=1:TNN
    NC_1(n,1)=NC(n,1)+U(2*n-1,1);
    NC_1(n,2)=NC(n,2)+U(2*n,1);
end

for n=1:EMI(1);
```

```
    if NC_1(((n-
1)*(EMI(2)*2+1)+1),1)>=NC_1(((n)*(EMI(2)*2+1)+1),1);
       IterationLoopGo=0;
       LoadStepLoopGo=0;
       LLS=LS-1;
    end
end

end %end Iteration loop

if Situation==1 && LS==NLS(1)
    [Fy,Uy]=MHA_FORCE(KG,U,NOHB);
    BUYLS=2*abs(mean(Uy));
    BFYLS=2*sum(Fy);
end

if Situation==2
    [Fy,Uy]=MHA_FORCE(KG,U,NOHB);
    UYLS(LS,1)=2*abs(mean(Uy));
    FYLS(LS,1)=2*sum(Fy);
end

if Situation==1
    NC_Results1(1:TNN,1:2,LS)=NC_1;
end
if Situation==2
    NC_Results2(1:TNN,1:2,LS)=NC_1;
end

end %end LS loop

end %end Situation loop

%create one array that contains the blocked displacement and force
along
%with dislacement and force for each expansion step
UY=vertcat(BUYLS,UYLS(1:LLS,1));
FY=vertcat(BFYLS,FYLS(1:LLS,1));

%create arrays that store the solution of the miniature hourglass
%actuator simulation
[PFY,PUY,FA,WA,PE,UFE,UEF,WMHA,WCTA]=MHA_WORK(FY,UY,NC,p,EMI);

%create arrays that contain the nodal coordinates of the undeformed
and
%deformed miniature hourglass actuator
[UDINC,UDONC,DINC,DONC]=MHA_FULL_COORDINATES(NC,NC_Results2(:,:,LLS
),EMI);

toc;
```

APPENDIX B

PRESSURE SIDE

A subroutine that creates an array containing the information of which regions elements will have pressure applied to their sides

```
function [PSide]=PressureSide(EMI)

NEAA=EMI(1);
NETA=EMI(2);
NEAB=EMI(3);
NETB=EMI(4);

PSide=zeros((NEAA*NETA+NETB*NETA+NEAB*NETB),1);
ElementCount=0;
for i=1:NEAA
    for j=1:NETA
        ElementCount=ElementCount+1;

        if j==1
        PSide(ElementCount,1)=4;
        end
    end
end

ElementCount=ElementCount+NETA*NETB;

for i=1:NETB
    for j=1:NEAB
        ElementCount=ElementCount+1;

        if i==1
        PSide(ElementCount,1)=3;
        end
    end
end

end
```

APPENDIX C

MHA MESH GENERATOR

Creates a element mesh and all corresponding information for a given MHA geometry

```
function [NC,NCA,DOFCA,NE,TNN,NOAS,NOAR,NOHIS,NOHB]=...

MHA_MESH_GENERATOR(Geometry,EMI)

r=Geometry(1);
t=Geometry(2);
alpha=Geometry(3);
R=Geometry(4);
T=Geometry(5);
%d=Geometry(6);

NE=EMI(1)*EMI(2)+EMI(4)*EMI(2)+EMI(3)*EMI(4);  %Number Of Elemets
TNN=(EMI(1)*2)*(EMI(2)*2+1)+(EMI(4)*2+1)*...
    (EMI(2)*2+1)+(EMI(3)*2)*(EMI(4)*2+1);
%Calculating The Hourglass Geometry

%Arc Bottom First Point Location
a=1;
b=-2*(r+t/2)*cos(pi-alpha/2);
c=(r+t/2)^2-(r+t)^2;

RAB1=R-(-b+sqrt(b^2-4*a*c))/(2*a);
%ZAB1=T;

%Arc Bottom Center Point Location
RAB2=R;
%ZAB2=T;

%Arc Bottom Last Point Location
a=1;
b=-2*(r+t/2)*cos(alpha/2);
c=(r+t/2)^2-(r)^2;

RAB3=R+(-b-sqrt(b^2-4*a*c))/(2*a);
%ZAB3=T;

%Center Of Arc Location
RCA=R+r*cos(alpha/2);
ZCA=T+r*sin(alpha/2);

%Arc Bottom Coordinates
RAB(1:2*EMI(2)*2/2+1)=zeros;
for i=1:EMI(2)*2/2
    RAB(i)=RAB1+(RAB2-RAB1)/EMI(2)*2/2*(i-1);
```

```
    RAB(i+EMI(2)*2/2)=RAB2+(RAB3-RAB2)/EMI(2)*2/2*(i-1);
    RAB(i+EMI(2)*2/2+1)=RAB3;
end
ZAB(1:2*EMI(2)*2/2+1)=T;


%Nodal Coordinates In Arc Region
Count=0;
RC(1:TNN,1)=zeros;
ZC(1:TNN,1)=zeros;
for i=1:EMI(1)*2
    for j=1:EMI(2)*2+1
        Count=Count+1;
        rt=(r+t/2-(j-1)*t/(EMI(2)*2+1-1));
        theta=atan((ZAB(j)-ZCA)/(RAB(j)-RCA))/(EMI(1)*2)*(i-1);
        RC(Count,1)=RCA-rt*cos(theta);
        ZC(Count,1)=ZCA-rt*sin(theta);
    end
end

%Nodal Coordinates Along the Bottom of The Arc Region
for j=1:EMI(2)*2+1
    Count=Count+1;
    RC(Count,1)=RAB(j);
    ZC(Count,1)=ZAB(j);
end

%Nodal Coordinates In Bottom Arc Region
for i=1:EMI(4)*2
    for j=1:EMI(2)*2+1
    Count=Count+1;
    RC(Count,1)=RAB(j);
    ZC(Count,1)=T-T/(EMI(4)*2)*i;
    end
end

%Nodal Coordinates In Bottom Non-Arc Region
for i=1:EMI(4)*2+1
    for j=1:EMI(3)*2
        Count=Count+1;
        RC(Count,1)=RAB1/(EMI(3)*2)*(j-1);
        ZC(Count,1)=T-T/(EMI(4)*2)*(i-1);
    end
end

%Nodal and Degree of Freedom Connectivity Arrays
ElementCount=0;
NCA(1:NE,1:9)=zeros;
for i=1:EMI(1)+EMI(4)
    for j=1:EMI(2)
        ElementCount=ElementCount+1;
```

```
        Nodes_r=2*EMI(2)+1;
        NextNode=[2*Nodes_r 2*Nodes_r+2 2 0 2*Nodes_r+1 Nodes_r+2 1
Nodes_r Nodes_r+1];

        for n=1:9
            NCA(ElementCount,n)=2*(i-1)*Nodes_r+1+2*(j-
1)+NextNode(n);
        end
    end
end

for i=1:EMI(4)
    for j=1:EMI(3)
        ElementCount=ElementCount+1;
        Nodes_r=2*EMI(3);
        NextNode=[2*Nodes_r 2*Nodes_r+2 2 0 2*Nodes_r+1 Nodes_r+2 1
Nodes_r Nodes_r+1];

        for n=1:9

NCA(ElementCount,n)=(2*EMI(2)+1)*(2*(EMI(1)+EMI(4))+1)+2*(i-
1)*(Nodes_r+1)+1+2*(j-1)+NextNode(n)-2*(i-1);

            if j==EMI(3)
            NCA(ElementCount,2)=(2*EMI(1))*(2*EMI(2)+1)+1+2*(i-
1)*(2*EMI(2)+1)+2*(2*EMI(2)+1);
            NCA(ElementCount,3)=(2*EMI(1))*(2*EMI(2)+1)+1+2*(i-
1)*(2*EMI(2)+1);
            NCA(ElementCount,6)=(2*EMI(1))*(2*EMI(2)+1)+1+2*(i-
1)*(2*EMI(2)+1)+(2*EMI(2)+1);
            end
        end
    end
end

DOFCA(1:NE,1:2*9)=zeros;
for i=1:NE
    for j=1:9
        for k=1:2
            DOFCA(i,(j-1)*2+k)=(NCA(i,j)-1)*2+k;
        end
    end
end

%Element Boundarys
RE(1:NE,1:9)=zeros;
ZE(1:NE,1:9)=zeros;
for i=1:NE
    for j=1:9
        NodeOrder=[1 5 2 6 3 7 4 8 1];
    RE(i,j)=RC(NCA(i,NodeOrder(j)),1);
```

```
    ZE(i,j)=ZC(NCA(i,NodeOrder(j)),1);
    end
end

%Nodes On Axis of Symmetry
NOAS_Count=0;
NOAS(1:(EMI(2)*2+1))=zeros;
for i=1:EMI(2)*2+1;
    NOAS_Count=NOAS_Count+1;
    NOAS(NOAS_Count)=i;
end

%Nodes On Axis of Revolution
NOAR_Count=0;
NOAR(1:(EMI(4)*2+1))=zeros;
for i=1:EMI(4)*2+1
    NOAR_Count=NOAR_Count+1;
    NOAR(NOAR_Count)=(2*EMI(2)+1)*(2*(EMI(1)+EMI(4))+1)+1+(i-
1)*(EMI(3)*2);
end

%Nodes On HCE Inner Surface
NOHIS_Count=0;
NOHIS(1:(EMI(1)*2+1+EMI(3)*2))=zeros;
for i=1:EMI(1)*2+1
    NOHIS_Count=NOHIS_Count+1;
    NOHIS(NOHIS_Count)=1+(i-1)*(EMI(2)*2+1);
end
for i=1:EMI(3)*2
    NOHIS_Count=NOHIS_Count+1;
    NOHIS(NOHIS_Count)=(2*EMI(2)+1)*(2*(EMI(1)+EMI(4))+1)+i;
end

%Nodes On HCE Bottom
NOHB_Count=0;
NOHB(1:(EMI(3)*2+EMI(2)*2+1))=zeros;
for i=1:EMI(3)*2
    NOHB_Count=NOHB_Count+1;

NOHB(NOHB_Count)=(2*EMI(2)+1)*(2*(EMI(1)+EMI(4))+1)+(EMI(3)*2)*(EMI
(4)*2)+i;
end
for i=1:EMI(2)*2+1
    NOHB_Count=NOHB_Count+1;
    NOHB(NOHB_Count)=(EMI(2)*2+1)*(2*(EMI(1)+EMI(4)))+i;
end

NC=[RC ZC];

end
```

APPENDIX D

BOUNDARY CONDITION

A subroutine that creates the necessary boundary condition information

```
function [DOFSPV,VSPV]=BoundaryCondition(NOAS,NOAR,NOHB)

DOFSPV_Count=0;
L=length(NOAS)+length(NOAR)+length(NOHB)-1;
DOFSPV=zeros(1,L);
VSPV=zeros(1,L);
for i=1:length(NOAS)
    DOFSPV_Count=DOFSPV_Count+1;
    DOFSPV(DOFSPV_Count)=NOAS(i)*2;
    VSPV(DOFSPV_Count)=0;
end

for i=1:length(NOAR)
    DOFSPV_Count=DOFSPV_Count+1;
    DOFSPV(DOFSPV_Count)=NOAR(i)*2-1;
    VSPV(DOFSPV_Count)=0;
end

for i=2:length(NOHB)
    DOFSPV_Count=DOFSPV_Count+1;
    DOFSPV(DOFSPV_Count)=NOHB(i)*2-1;
    VSPV(DOFSPV_Count)=0;
end
```

APPENDIX E

STEPPED BOTTOM DISPLACEMENT BC

A subroutine that creates an array containing the degrees of freedom along the MHA bottom that will undergo displacement steps

```
function [DOFSBD,VSBD]=SteppedBottomDisplacementBC(NOHB)

DOFSBD(length(NOHB))=zeros;
VSBD(length(NOHB))=zeros;

for i=1:length(NOHB)
    DOFSBD(i)=2*NOHB(i);
end
```

APPENDIX F

ELEMENT STIFFNESS FOR UPDATED LAGRANGIAN

A subroutine that creates the element stiffness matrices with the updated Lagrangian formulation

```
function
[KE]=ElementStiffnes4UpdatedLagrangian(E,NCA,DOFCA,NC,U,ETI,Materia
l,d)

Ey=Material(1);
v=Material(2);
SS=Material(3);

ET=ETI(1);
NDOFPN=ETI(2);
NNPE=ETI(3);
NGP=ETI(4);

%Plane Stress
    if SS==1
    C11_1=Ey/(1-v^2);
    C12_1=Ey*v/(1-v^2);
    C22_1=Ey/(1-v^2);
    C66_1=Ey/(2*(1+v));
    end

%Plane Strain
    if SS==2
    C11_1=Ey*(1-v)/((1+v)*(1-2*v));
    C12_1=Ey*v/((1+v)*(1-2*v));
    C22_1=C11_1;
    C66_1=Ey/(2*(1+v));
    end

K11L=zeros(NNPE);
K12L=zeros(NNPE);
K22L=zeros(NNPE);
K11N=zeros(NNPE);

for i=1:NNPE
    for j=1:NNPE
        for m=1:NGP
            for n=1:NGP

    [psi,dpsi_dxi,dpsi_deta,GPC,GPW]=Interpolation(ET,NGP,m,n);
    [J11,J12,J21,J22,DetJ]=Jacobain;

    dpsii_dx=(J22*dpsi_dxi(i)-J12*dpsi_deta(i))/DetJ;
```

```
    dpsij_dx=(J22*dpsi_dxi(j)-J12*dpsi_deta(j))/DetJ;
    dpsii_dy=(-J21*dpsi_dxi(i)+J11*dpsi_deta(i))/DetJ;
    dpsij_dy=(-J21*dpsi_dxi(j)+J11*dpsi_deta(j))/DetJ;

    dxdy=DetJ*GPW(m)*GPW(n);


K11L(i,j)=K11L(i,j)+d*(C11_1*dpsii_dx*dpsij_dx+C66_1*dpsii_dy*dpsij
_dy)*dxdy;
K12L(i,j)=K12L(i,j)+d*(C12_1*dpsii_dx*dpsij_dy+C66_1*dpsii_dy*dpsij
_dx)*dxdy;
K22L(i,j)=K22L(i,j)+d*(C66_1*dpsii_dx*dpsij_dx+C22_1*dpsii_dy*dpsij
_dy)*dxdy;


    du_dx=0; dv_dx=0; du_dy=0; dv_dy=0;
    for p=1:NNPE
    du_dx=du_dx+U(DOFCA(E,(2*p-1)),1)*(J22*dpsi_dxi(p)-
J12*dpsi_deta(p))/DetJ;
    dv_dx=dv_dx+U(DOFCA(E,(2*p)),1)*(J22*dpsi_dxi(p)-
J12*dpsi_deta(p))/DetJ;
    du_dy=du_dy+U(DOFCA(E,(2*p-1)),1)*(-
J21*dpsi_dxi(p)+J11*dpsi_deta(p))/DetJ;
    dv_dy=dv_dy+U(DOFCA(E,(2*p)),1)*(-
J21*dpsi_dxi(p)+J11*dpsi_deta(p))/DetJ;
    end


    sigmaxx_1=C11_1*(du_dx-(1/2)*(du_dx^2+dv_dx^2))+C12_1*(dv_dy-
(1/2)*(du_dy^2+dv_dy^2));
    sigmaxy_1=C66_1*(du_dy+dv_dx-(du_dx*du_dy+dv_dx*dv_dy));
    sigmayy_1=C12_1*(du_dx-(1/2)*(du_dx^2+dv_dx^2))+C22_1*(dv_dy-
(1/2)*(du_dy^2+dv_dy^2));

K11N(i,j)=K11N(i,j)+d*(sigmaxx_1*dpsii_dx*dpsij_dx+sigmaxy_1*(dpsii
_dy*dpsij_dx+dpsii_dx*dpsij_dy)+sigmayy_1*dpsii_dy*dpsij_dy)*dxdy;

            end
        end
    end
end
K21L=K12L';
K22N=K11N;

K=[(K11L+K11N) K12L;K21L (K22L+K22N)];

%rearrange the element stiffness matrix
switch NNPE
    case 4
        N=[1 5 2 6 3 7 4 8];
    case 9
```

```
        N=[1 10 2 11 3 12 4 13 5 14 6 15 7 16 8 17 9 18];
end

    KE=zeros(NNPE*NDOFPN,NNPE*NDOFPN);
    for i=1:NNPE*NDOFPN
        for j=1:NNPE*NDOFPN
        KE(i,j)=K(N(i),N(j));
        end %end j loop
    end %end i loop

            function [J11,J12,J21,J22,DetJ]=Jacobain
            %Jacobian evaluated at the Gauss points
            J11=0; J12=0; J21=0; J22=0;
                    for k=1:NNPE
                    J11=J11+dpsi_dxi(k)*NC(NCA(E,k),1);
                    J12=J12+dpsi_dxi(k)*NC(NCA(E,k),2);
                    J21=J21+dpsi_deta(k)*NC(NCA(E,k),1);
                    J22=J22+dpsi_deta(k)*NC(NCA(E,k),2);
                    DetJ=J11*J22-J12*J21;
                    end %end n loop
            end %end Jacobian
end
```

APPENDIX G

ELEMENT FORCE FOR UPDATED LAGRANGIAN

A subroutine that creates the element force matrices with the updated Lagrangian formulation

```
function
[FE]=ElementForce4UpdatedLagrangian(E,NCA,DOFCA,NC,U,P,d,ETI,Materi
al,PSide)

Ey=Material(1);
v=Material(2);
SS=Material(3);

ET=ETI(1);
NDOFPN=ETI(2);
NNPE=ETI(3);
NGP=ETI(4);

%Plane Stress
    if SS==1
    C11_1=Ey/(1-v^2);
    C12_1=Ey*v/(1-v^2);
    C22_1=Ey/(1-v^2);
    C66_1=Ey/(2*(1+v));
    end

%Plane Strain
    if SS==2
    C11_1=Ey*(1-v)/((1+v)*(1-2*v));
    C12_1=Ey*v/((1+v)*(1-2*v));
    C22_1=C11_1;
    C66_1=Ey/(2*(1+v));
    end


F1_11=zeros(NNPE,1);
F2_11=zeros(NNPE,1);

for i=1:NNPE
    for m=1:NGP
        for n=1:NGP

        [psi,dpsi_dxi,dpsi_deta,GPC,GPW]=Interpolation(ET,NGP,m,n);
        [J11,J12,J21,J22,DetJ]=Jacobain;

        dpsii_dx=(J22*dpsi_dxi(i)-J12*dpsi_deta(i))/DetJ;
        dpsii_dy=(-J21*dpsi_dxi(i)+J11*dpsi_deta(i))/DetJ;
```

```
        dxdy=DetJ*GPW(m)*GPW(n);

        du_dx=0; dv_dx=0; du_dy=0; dv_dy=0;
    for p=1:NNPE
    du_dx=du_dx+U(DOFCA(E,(2*p-1)),1)*(J22*dpsi_dxi(p)-
J12*dpsi_deta(p))/DetJ;
    dv_dx=dv_dx+U(DOFCA(E,(2*p)),1)*(J22*dpsi_dxi(p)-
J12*dpsi_deta(p))/DetJ;
    du_dy=du_dy+U(DOFCA(E,(2*p-1)),1)*(-
J21*dpsi_dxi(p)+J11*dpsi_deta(p))/DetJ;
    dv_dy=dv_dy+U(DOFCA(E,(2*p)),1)*(-
J21*dpsi_dxi(p)+J11*dpsi_deta(p))/DetJ;
    end


    sigmaxx_1=C11_1*(du_dx-(1/2)*(du_dx^2+dv_dx^2))+C12_1*(dv_dy-
(1/2)*(du_dy^2+dv_dy^2));
    sigmaxy_1=C66_1*(du_dy+dv_dx-(du_dx*du_dy+dv_dx*dv_dy));
    sigmayy_1=C12_1*(du_dx-(1/2)*(du_dx^2+dv_dx^2))+C22_1*(dv_dy-
(1/2)*(du_dy^2+dv_dy^2));


F1_11(i)=F1_11(i)+d*(dpsii_dx*sigmaxx_1+dpsii_dy*sigmaxy_1)*dxdy;

F2_11(i)=F2_11(i)+d*(dpsii_dx*sigmaxy_1+dpsii_dy*sigmayy_1)*dxdy;

        end
    end
end

[F1_21,F2_21]=MHA_PRESSURE(P,E,NC,NCA,NGP,PSide);

F=[(F1_21-F1_11);(F2_21-F2_11)];


switch NNPE
    case 4
        N=[1 5 2 6 3 7 4 8];
    case 9
        N=[1 10 2 11 3 12 4 13 5 14 6 15 7 16 8 17 9 18];
end

FE=zeros(NNPE*NDOFPN,1);
for i=1:NNPE*NDOFPN
    FE(i)=F(N(i));
end %end i loop

            function [J11,J12,J21,J22,DetJ]=Jacobain
            %Jacobian evaluated at the Gauss points
            J11=0; J12=0; J21=0; J22=0;
                    for k=1:NNPE
```

```
                J11=J11+dpsi_dxi(k)*NC(NCA(E,k),1);
                J12=J12+dpsi_dxi(k)*NC(NCA(E,k),2);
                J21=J21+dpsi_deta(k)*NC(NCA(E,k),1);
                J22=J22+dpsi_deta(k)*NC(NCA(E,k),2);
                DetJ=J11*J22-J12*J21;
                end %end n loop
        end %end Jacobian

end
```

APPENDIX H

MHA PRESSURE

A subroutine that creates that calculates the direction and magnitude of the forces on the element sides from the pressure

```
function [F1_21,F2_21]=MHA_PRESSURE(P,E,NC,NCA,NGP,PSide)

F1=zeros(9,1);
F2=zeros(9,1);

if PSide(E,1)~=0;
x=zeros(9);
y=zeros(9);

[GPC,GPW]=GaussPointCoordinateandWeight(NGP);

for m=1:9
    x(m)=NC(NCA(E,m),1);
    y(m)=NC(NCA(E,m),2);
end
    for j=1:3 %Number of Nodes per Element side

            if PSide(E,1)==1; Nodes=[1 5 2]; eta=-1; end
            if PSide(E,1)==2; Nodes=[2 6 3]; xi=1; end
            if PSide(E,1)==3; Nodes=[3 7 4]; eta=1; end
            if PSide(E,1)==4; Nodes=[4 8 1]; xi=-1; end

        for k=1:NGP

            if PSide(E,1)==1; xi=GPC(k); end
            if PSide(E,1)==2; eta=GPC(k); end
            if PSide(E,1)==3; xi=GPC(k); end
            if PSide(E,1)==4; eta=GPC(k); end


                                psi(1)=(1/4)*(xi^2-xi)*(eta^2-eta);
                                psi(2)=(1/4)*(xi^2+xi)*(eta^2-eta);
                                psi(3)=(1/4)*(xi^2+xi)*(eta^2+eta);
                                psi(4)=(1/4)*(xi^2-xi)*(eta^2+eta);
                                psi(5)=(1/2)*(1-xi^2)*(eta^2-eta);
                                psi(6)=(1/2)*(xi^2+xi)*(1-eta^2);
                                psi(7)=(1/2)*(1-xi^2)*(eta^2+eta);
                                psi(8)=(1/2)*(xi^2-xi)*(1-eta^2);
                                psi(9)=(1-xi^2)*(1-eta^2);

                                dpsi_dxi(1)=(1/4)*(2*xi-1)*(eta^2-eta);
                                dpsi_dxi(2)=(1/4)*(2*xi+1)*(eta^2-eta);
                                dpsi_dxi(3)=(1/4)*(2*xi+1)*(eta^2+eta);
```

```
                                dpsi_dxi(4)=(1/4)*(2*xi-1)*(eta^2+eta);
                                dpsi_dxi(5)=-xi*(eta^2-eta);
                                dpsi_dxi(6)=(1/2)*(2*xi+1)*(1-eta^2);
                                dpsi_dxi(7)=-xi*(eta^2+eta);
                                dpsi_dxi(8)=(1/2)*(2*xi-1)*(1-eta^2);
                                dpsi_dxi(9)=-2*xi*(1-eta^2);

                                dpsi_deta(1)=(1/4)*(xi^2-xi)*(2*eta-1);
                                dpsi_deta(2)=(1/4)*(xi^2+xi)*(2*eta-1);
                                dpsi_deta(3)=(1/4)*(xi^2+xi)*(2*eta+1);
                                dpsi_deta(4)=(1/4)*(xi^2-xi)*(2*eta+1);
                                dpsi_deta(5)=(1/2)*(1-xi^2)*(2*eta-1);
                                dpsi_deta(6)=-(xi^2+xi)*eta;
                                dpsi_deta(7)=(1/2)*(1-xi^2)*(2*eta+1);
                                dpsi_deta(8)=-(xi^2-xi)*eta;
                                dpsi_deta(9)=-2*(1-xi^2)*eta;


        dx_dxi=0;
        dy_dxi=0;
        dx_deta=0;
        dy_deta=0;

for n=1:9
    dx_dxi=dx_dxi+x(n)*dpsi_dxi(n);
    dy_dxi=dy_dxi+y(n)*dpsi_dxi(n);

    dx_deta=dx_deta+x(n)*dpsi_deta(n);
    dy_deta=dy_deta+y(n)*dpsi_deta(n);
end

ds_dxi=sqrt(dx_dxi^2+dy_dxi^2);
ds_deta=sqrt(dx_deta^2+dy_deta^2);

if PSide(E,1)==1 %side where eta=-1
    nx=dy_dxi/sqrt(dx_dxi^2+dy_dxi^2);
    ny=-dx_dxi/sqrt(dx_dxi^2+dy_dxi^2);

    F1(Nodes(j),1)=F1(Nodes(j),1)-P*psi(Nodes(j))*nx*ds_dxi*GPW(k);
    F2(Nodes(j),1)=F2(Nodes(j),1)-P*psi(Nodes(j))*ny*ds_dxi*GPW(k);
end

if PSide(E,1)==2 %side where xi=1
    nx=dy_deta/sqrt(dx_deta^2+dy_deta^2);
    ny=-dx_deta/sqrt(dx_deta^2+dy_deta^2);

    F1(Nodes(j),1)=F1(Nodes(j),1)-
P*psi(Nodes(j))*nx*ds_deta*GPW(k);
    F2(Nodes(j),1)=F2(Nodes(j),1)-
P*psi(Nodes(j))*ny*ds_deta*GPW(k);
end
```

```
if PSide(E,1)==3 %side where eta=1
    nx=-dy_dxi/sqrt(dx_dxi^2+dy_dxi^2);
    ny=dx_dxi/sqrt(dx_dxi^2+dy_dxi^2);

    F1(Nodes(j),1)=F1(Nodes(j),1)-P*psi(Nodes(j))*nx*ds_dxi*GPW(k);
    F2(Nodes(j),1)=F2(Nodes(j),1)-P*psi(Nodes(j))*ny*ds_dxi*GPW(k);
end

if PSide(E,1)==4 %side where xi=-1
    nx=-dy_deta/sqrt(dx_deta^2+dy_deta^2);
    ny=dx_deta/sqrt(dx_deta^2+dy_deta^2);

    F1(Nodes(j),1)=F1(Nodes(j),1)-
P*psi(Nodes(j))*nx*ds_deta*GPW(k);
    F2(Nodes(j),1)=F2(Nodes(j),1)-
P*psi(Nodes(j))*ny*ds_deta*GPW(k);
end

        end
    end

end
    F1_21=F1;
    F2_21=F2;
end
```

APPENDIX I

INTERPOLATION

A subroutine that contains the interpolation functions and their derivatives

```
function [psi,dpsi_dxi,dpsi_deta,GPC,GPW]=Interpolation(ET,NGP,m,n)

[GPC,GPW]=GaussPointCoordinateandWeight(NGP);

if ET==1

xi=GPC(m);
eta=GPC(n);

psi(1)=(1-xi)*(1-eta)/4;
psi(2)=(1+xi)*(1-eta)/4;
psi(3)=(1+xi)*(1+eta)/4;
psi(4)=(1-xi)*(1+eta)/4;

dpsi_dxi(1)=-(1/4)*(1-eta);
dpsi_dxi(2)=(1/4)*(1-eta);
dpsi_dxi(3)=(1/4)*(1+eta);
dpsi_dxi(4)=-(1/4)*(1+eta);

dpsi_deta(1)=-(1/4)*(1-xi);
dpsi_deta(2)=-(1/4)*(1+xi);
dpsi_deta(3)=(1/4)*(1+xi);
dpsi_deta(4)=(1/4)*(1-xi);

end %end if linear elements

%for quadratic elemnts
if ET==2

xi=GPC(m);
eta=GPC(n);

psi(1)=(1/4)*(xi^2-xi)*(eta^2-eta);
psi(2)=(1/4)*(xi^2+xi)*(eta^2-eta);
psi(3)=(1/4)*(xi^2+xi)*(eta^2+eta);
psi(4)=(1/4)*(xi^2-xi)*(eta^2+eta);
psi(5)=(1/2)*(1-xi^2)*(eta^2-eta);
psi(6)=(1/2)*(xi^2+xi)*(1-eta^2);
psi(7)=(1/2)*(1-xi^2)*(eta^2+eta);
psi(8)=(1/2)*(xi^2-xi)*(1-eta^2);
psi(9)=(1-xi^2)*(1-eta^2);

dpsi_dxi(1)=(1/4)*(2*xi-1)*(eta^2-eta);
dpsi_dxi(2)=(1/4)*(2*xi+1)*(eta^2-eta);
```

```
dpsi_dxi(3)=(1/4)*(2*xi+1)*(eta^2+eta);
dpsi_dxi(4)=(1/4)*(2*xi-1)*(eta^2+eta);
dpsi_dxi(5)=-xi*(eta^2-eta);
dpsi_dxi(6)=(1/2)*(2*xi+1)*(1-eta^2);
dpsi_dxi(7)=-xi*(eta^2+eta);
dpsi_dxi(8)=(1/2)*(2*xi-1)*(1-eta^2);
dpsi_dxi(9)=-2*xi*(1-eta^2);

dpsi_deta(1)=(1/4)*(xi^2-xi)*(2*eta-1);
dpsi_deta(2)=(1/4)*(xi^2+xi)*(2*eta-1);
dpsi_deta(3)=(1/4)*(xi^2+xi)*(2*eta+1);
dpsi_deta(4)=(1/4)*(xi^2-xi)*(2*eta+1);
dpsi_deta(5)=(1/2)*(1-xi^2)*(2*eta-1);
dpsi_deta(6)=-(xi^2+xi)*eta;
dpsi_deta(7)=(1/2)*(1-xi^2)*(2*eta+1);
dpsi_deta(8)=-(xi^2-xi)*eta;
dpsi_deta(9)=-2*(1-xi^2)*eta;

end %end if quadratic elements

% 8 node serendipity element
if ET==3

xi=GPC(m);
eta=GPC(n);

psi(1)=-1/4*(1-xi)*(1-eta)*(1+xi+eta);
psi(2)=-1/4*(1+xi)*(1-eta)*(1-xi+eta);
psi(3)=-1/4*(1+xi)*(1+eta)*(1-xi-eta);
psi(4)=-1/4*(1-xi)*(1+eta)*(1+xi-eta);
psi(5)=1/2*(1-xi^2)*(1-eta);
psi(6)=1/2*(1+xi)*(1-eta^2);
psi(7)=1/2*(1-xi^2)*(1+eta);
psi(8)=1/2*(1-xi)*(1-eta^2);

dpsi_dxi(1)=xi/2-xi*eta/2+(eta^2)/4-eta/4;
dpsi_dxi(2)=xi/2-xi*eta/2+(eta^2)/4-eta/4;
dpsi_dxi(3)=xi/2+xi*eta/2+(eta^2)/4+eta/4;
dpsi_dxi(4)=xi*(-1+eta);
dpsi_dxi(5)=xi*(-1+eta);
dpsi_dxi(6)=1/2-(eta^2)/2;
dpsi_dxi(7)=-xi*(1+eta);
dpsi_dxi(8)=-1/2+(eta^2)/2;

dpsi_deta(1)=eta/2-(xi^2)/4+eta*xi/2-xi/4;
dpsi_deta(2)=eta/2-(xi^2)/4+eta*xi/2-xi/4;
dpsi_deta(3)=eta/2+(xi^2)/4+eta*xi/2+xi/4;
dpsi_deta(4)=-1/2+(xi^2)/2;
dpsi_deta(5)=-1/2+(xi^2)/2;
dpsi_deta(6)=-(1+xi)*eta;
dpsi_deta(7)=1/2-(xi^2)/2;
```

```
dpsi_deta(8)=(-1+xi)*eta;

end %end if 8 node serendipity element

end
```

APPENDIX J

GAUSS POINT COORDINATE AND WEIGHT

A subroutine that contains the Gauss point coordinates and weights

```
function [GPC,GPW]=GaussPointCoordinateandWeight(NGP)

%Gauss Point Coordinate and Weight Arrays

switch NGP

    case 1
        GPC=(0.0);
        GPW=(2);

    case 2
        GPC=[-1/sqrt(3) 1/sqrt(3)];
        GPW=[1 1];

    case 3
        GPC=[-sqrt(3/5) 0 sqrt(3/5)];
        GPW=[5/9 8/9 5/9];

    case 4
        GPC=[-sqrt((3+2*sqrt(6/5))/7) -sqrt((3-2*sqrt(6/5))/7) ...
              sqrt((3-2*sqrt(6/5))/7) sqrt((3+2*sqrt(6/5))/7)];
        GPW=[(18-sqrt(30))/36 (18+sqrt(30))/36 (18+sqrt(30))/36 ...
             (18-sqrt(30))/36];
    case 5
        GPC=[-1/3*sqrt(5+2*sqrt(10/7)) -1/3*sqrt(5-2*sqrt(10/7)) 0
...
              1/3*sqrt(5-2*sqrt(10/7)) 1/3*sqrt(5+2*sqrt(10/7))];
        GPW=[(322-13*sqrt(70))/900 (322+13*sqrt(70))/900 128/225
...
             (322+13*sqrt(70))/900 (322-13*sqrt(70))/900];

    otherwise
        disp(['No Gauss point cooridnates or weights are
available'...
              'for more than 5 Gauss points'])

end

end
```

APPENDIX K

MHA FORCE

A subroutine that calculates the force on the bottom surface of the MHA

```
function [Fy,Uy]=MHA_FORCE(KG,U,NOHB)

%Fx=zeros(length(NOHB),1);
Fy=zeros(length(NOHB),1);
Uy=zeros(length(NOHB),1);

%find the force acting on the miniature hourglass actuator
for i=1:length(NOHB)

    %Fx(i,1)=KG(2*NOHB(i)-1,:)*U;
    Fy(i,1)=KG(2*NOHB(i),:)*U;
    Uy(i,1)=U(2*NOHB(i),1);

end

%none of the forces in the x direction are calculated

end
```

APPENDIX L

MHA WORK

A subroutine that calculates the work density of the MHA along with its force and work advantages

```
function
[PFY,PUY,FA,WA,PE,UFE,UEF,WMHA,WCTA]=MHA_WORK(FY,UY,NC,p,EMI)

%element mesh information
NEAA=EMI(1);
NETA=EMI(2);
%NEAB=EMI(3);
NETB=EMI(4);

%find the all of displacements where the force is positive
RFY=find(FY>0);
PFY=FY(1:length(RFY),1);
PUY=UY(1:length(RFY),1);

%find the displacement u where the force is zero by linealy
interpolation
UFE=UY(length(RFY),1);
PFY=vertcat(PFY,0);
PUY=vertcat(PUY,UFE);

%find the force on the MHA bottom
RT=(NETA*2+1)*(NEAA*2)+1;
LT=(NETA*2+1)*((NEAA+NETB)*2+1)+1;
BL=2*(NC(RT,1)-NC(LT,1));
BF=BL*p;

W=0;
for i=1:length(PUY)-1
    W=W+(PFY(i)+PFY(i+1))/2*(PUY(i+1)-PUY(i));
end

%calculate the total outside area of the miniature hourglass
actuator
BR=(NETA*2+1)*((NEAA+NETB)*2+1);
TR=NETA*2+1;
OUA=4*(NC(BR,1)*NC(TR,2));

%calculate the work done by both the miniature hourglass actuator
and a
%compariable traditional actuator
WMHA=W/OUA;
WCTA=BF*UFE/OUA;
```

```
%the initial blocked force of both the miniature hourglass actuator
and a
%compariable traditional actuator
FMHA=PFY(1,1);
FCTA=BF;

%find the force and work advantage
FA=FMHA/FCTA;
WA=WMHA/WCTA;

%calculate the percent elogation
PE=UFE/NC(1,2)*100; -This line is should be PE=UFE/(2*NC(1,2))*100;

%calculate the elongation where the force of the miniature
hourglass
%actuator is equal to the force of the compariable traditional
actuator
if FA>1 && PFY(length(PFY-1),1)<FCTA
    REFFY=find(PFY>FCTA);

    UEF=PUY(length(REFFY),1)+(FCTA-PFY(length(REFFY),1))/...
    ((PFY(length(REFFY)+1,1)-PFY(length(REFFY),1))/...
        (PUY(length(REFFY)+1,1)-PUY(length(REFFY),1)));
else
    UEF=0;
end

end
```

APPENDIX M

MHA FULL COORDINATES

A subroutine that takes the coordinates of the computational domain and creates an array of coordinates for the whole MHA

```
function [UDINC,UDONC,DINC,DONC]=MHA_FULL_COORDINATES(NC,NC_1,EMI)

%element mesh information
NEAA=EMI(1);
NETA=EMI(2);
NEAB=EMI(3);
NETB=EMI(4);


%find the nodes on the inner and outter sufaces
IS2=zeros(NEAA*2+1,1);
OS4=zeros(NEAA*2+1,1);
for i=1:NEAA*2+1
    IS2(i,1)=(NETA*2+1)*(NEAA*2)+1-(i-1)*(NETA*2+1);
    OS4(i,1)=(NETA*2+1)*(NEAA*2+1)-(i-1)*(NETA*2+1);
end

OS3=zeros(NETB*2,1);
for i=1:NETB*2
    OS3(i,1)=(NETA*2+1)*((NEAA+NETB)*2+1)-(i-1)*(NETA*2+1);
end

OS2=zeros(NETA*2,1);
for i=1:NETA*2
    OS2(i,1)=(NETA*2+1)*((NEAA+NETB)*2)+i;
end

IS1=zeros(NEAB*2,1);
OS1=zeros(NEAB*2,1);
for i=1:NEAB*2
    IS1(i,1)=(NETA*2+1)*((NEAA+NETB)*2+1)+i;
    OS1(i,1)=(NETA*2+1)*((NEAA+NETB)*2+1)+(NEAB*2)*(NETB*2)+i;
end

IS=[IS1;IS2];
OS=[OS1;OS2;OS3;OS4];

%put the nodes on the inner surface in order
ISx1=zeros(length(IS),1);ISx2=zeros(length(IS),1);
ISx3=zeros(length(IS),1);ISx4=zeros(length(IS),1);
ISy1=zeros(length(IS),1);ISy2=zeros(length(IS),1);
ISy3=zeros(length(IS),1);ISy4=zeros(length(IS),1);
```

```
for i=1:length(IS)
    n=length(IS)-i+1;
    ISx1(i)=NC(IS(i,1),1);
    ISx2(n)=NC(IS(i,1),1);
    ISx3(i)=-NC(IS(i,1),1);
    ISx4(n)=-NC(IS(i,1),1);
    ISy1(i)=NC(IS(i,1),2);
    ISy2(n)=2*NC(1,2)-NC(IS(i,1),2);
    ISy3(i)=2*NC(1,2)-NC(IS(i,1),2);
    ISy4(n)=NC(IS(i,1),2);
end

ISX=[ISx1;ISx2;ISx3;ISx4];
ISY=[ISy1;ISy2;ISy3;ISy4];

%put the nodes on the outter surface in order
OSx1=zeros(length(OS),1);OSx2=zeros(length(OS),1);
OSx3=zeros(length(OS),1);OSx4=zeros(length(OS),1);
OSy1=zeros(length(OS),1);OSy2=zeros(length(OS),1);
OSy3=zeros(length(OS),1);OSy4=zeros(length(OS),1);

for i=1:length(OS)
    n=length(OS)-i+1;
    OSx1(i)=NC(OS(i,1),1);
    OSx2(n)=NC(OS(i,1),1);
    OSx3(i)=-NC(OS(i,1),1);
    OSx4(n)=-NC(OS(i,1),1);
    OSy1(i)=NC(OS(i,1),2);
    OSy2(n)=2*NC(1,2)-NC(OS(i,1),2);
    OSy3(i)=2*NC(1,2)-NC(OS(i,1),2);
    OSy4(n)=NC(OS(i,1),2);
end

OSX=[OSx1;OSx2;OSx3;OSx4];
OSY=[OSy1;OSy2;OSy3;OSy4];

%find the inner surface nodal coordiates of the defoemed miniature
%hourglass actuator
DISx1=zeros(length(IS),1);DISx2=zeros(length(IS),1);
DISx3=zeros(length(IS),1);DISx4=zeros(length(IS),1);
DISy1=zeros(length(IS),1);DISy2=zeros(length(IS),1);
DISy3=zeros(length(IS),1);DISy4=zeros(length(IS),1);

for i=1:length(IS)
    n=length(IS)-i+1;
    DISx1(i)=NC_1(IS(i,1),1);
    DISx2(n)=NC_1(IS(i,1),1);
    DISx3(i)=-NC_1(IS(i,1),1);
    DISx4(n)=-NC_1(IS(i,1),1);
    DISy1(i)=NC_1(IS(i,1),2);
    DISy2(n)=2*NC(1,2)-NC_1(IS(i,1),2);
```

```
    DISy3(i)=2*NC(1,2)-NC_1(IS(i,1),2);
    DISy4(n)=NC_1(IS(i,1),2);
end

%find the outter surface nodal coordiates of the defoemed miniature
%hourglass actuator
DOSx1=zeros(length(OS),1);DOSx2=zeros(length(OS),1);
DOSx3=zeros(length(OS),1);DOSx4=zeros(length(OS),1);
DOSy1=zeros(length(OS),1);DOSy2=zeros(length(OS),1);
DOSy3=zeros(length(OS),1);DOSy4=zeros(length(OS),1);

for i=1:length(OS)
    n=length(OS)-i+1;
    DOSx1(i)=NC_1(OS(i,1),1);
    DOSx2(n)=NC_1(OS(i,1),1);
    DOSx3(i)=-NC_1(OS(i,1),1);
    DOSx4(n)=-NC_1(OS(i,1),1);
    DOSy1(i)=NC_1(OS(i,1),2);
    DOSy2(n)=2*NC(1,2)-NC_1(OS(i,1),2);
    DOSy3(i)=2*NC(1,2)-NC_1(OS(i,1),2);
    DOSy4(n)=NC_1(OS(i,1),2);
end

DISX=[DISx1;DISx2;DISx3;DISx4];
DISY=[DISy1;DISy2;DISy3;DISy4];
DOSX=[DOSx1;DOSx2;DOSx3;DOSx4];
DOSY=[DOSy1;DOSy2;DOSy3;DOSy4];

%shift the deformed miniature hourglass actuator up so that all the
%deformation is positive
n=(NETA*2+1)*((NEAA+NETB)*2+1)+(NEAB*2)*(NETB*2)+1;
MDISY=DISY-NC_1(n,2);
MDOSY=DOSY-NC_1(n,2);

%create arrays that contain both the x and y coordinates
DINC=horzcat(DISX,MDISY);
DONC=horzcat(DOSX,MDOSY);

UDINC=horzcat(ISX,ISY);
UDONC=horzcat(OSX,OSY);

end
```

VITA

Name: Roston Clement Elwell

Address: Texas A&M University
Department of Mechanical Engineering c/o Dr. Terry Creasy
3123 TAMU
College Station , TX 77843-3123

Email Address: roston.elwell@gmail.com

Education: B.S., Mechanical Engineering, California State Polytechnic University Pomona, 2006

M.S., Mechanical Engineering, Texas A&M University, 2010